M Sc Degree project 30 ECTS credits
Performed at the Nordic Volcanological Center,
Institute of Earth Sciences, University of Iceland
and Department of Physics, Umeå University, Sweden

February 2008

Eva Karlsson

Finite element modeling of Holocene deformation corresponding to Thingvellir graben, Iceland, in relation to spreading rate and rheology

M Sc Degree project 30 ECTS credits
Performed at the Nordic Volcanological Center,
Institute of Earth Sciences, University of Iceland
and Department of Physics, Umeå University, Sweden

February 2008

Eva Karlsson

Finite element modeling of Holocene deformation corresponding to Thingvellir graben, Iceland, in relation to spreading rate and rheology

Supervisor: Freysteinn Sigmundsson, Nordic Volcanological Center,
Institute of Earth Sciences, University of Iceland

Examiner: Páll Einarsson,
Institute of Earth Sciences, University of Iceland

Finite element modeling of Holocene deformation corresponding to Thingvellir graben, Iceland, in relation to spreading rate and rheology

ISBN 978-9979-9633-3-2
Printed by Oddi

This thesis can also be referred to as
Nordic Volcanological Center, Institute of Earth Sciences,
University of Iceland, Report 0802

Abstract

The formation of graben structures at extensional rifts is the central part of this study and especially the role of plate movements. Thingvellir, in the Western Volcanic Zone (WVZ) in Iceland, is used as a site to explore the process of graben formations. In the WVZ, few volcanic eruptions have occurred in postglacial time, except for the very early part of it, and a pronounced graben (Thingvellir graben) has formed. This study investigates if subsidence in the Thingvellir graben can be explained mainly as a consequence of stretching across the plate boundary and the lack of magma infill. For this purpose a two-dimensional model was constructed in the Abaqus finite element package. GPS-measured spreading rates and fault throws were used as constraints. Spreading rate is about 7 mm/yr at Thingvellir and fault offsets in the inner part of the graben suggest a minimum postglacial subsidence of 30 m. Three sets of end-member models that incorporate only stretching of the plate were tested with varying rheologies and layer configurations. Faulting and dike injections were not considered. The models were all subjected to a constant horizontal pull of 7 mm/yr over a distance of 20 km during 10 000 yrs which is about equivalent to the observed spreading rate at Thingvellir today. The results show that a curved boundary layer between an upper elastic layer and a lower viscoelastic layer, is essential to create a relative subsidence of the plate; hence with a horizontal boundary between different rheologies there is only uniform subsidence. The maximum relative subsidence achieved is about 25–35 m, for the elastic-viscoelastic model, as well as for a model with temperature dependent rheology. Plate stretching, considering realistic rheology, may thus have large influence on graben formation at magma-starved rifts. The modeled subsidence varies approximately linearly with spreading rate. This is in accordance with the observed decrease of spreading rate, as well as decrease of topographic relief towards the northeastern part of the Thingvellir graben. Shear stress distribution in the models suggests an elastic thickness at the ridge axis at Lake Thingvallavatn of about 3 km, thickening towards northeast.

Acknowledgments

First of all I would like to thank my supervisor Freysteinn Sigmundsson, who has generously provided me with inspiration as well as expertise. Secondly, Rósa Ólafsdóttir and Amy Clifton for help with maps and GIS related tasks. Rikke Pedersen, thank you for taking you time and introducing me to Abaqus. It was great help. I also want to thank Erik Sturkell for lending me his offices as well as Björn Lund at the Swedish National Seismic Network, for letting me use his office during the time in Uppsala. Finally, I would also like to thank the other people at the Earth Sciences Institute, University of Iceland, for a nice time here.

Takk fyrir!

Contents

1 Introduction 1

1.1 Aim of the project 3

2 Geological background 6

2.1 Eruptive history 7

2.2 Thingvellir graben 8

2.3 Lake Thingvallavatn 10

3 Crustal deformation and faulting 12

3.1 Constraints on vertical displacements 14

3.2 Constraints on horizontal displacements 16

4 Rheological models of a divergent plate boundary 20

4.1 Uniform elastic thickness 20

4.2 Curved elastic-viscoelastic boundary 21

4.3 Temperature dependent rheology 22

5 Finite element modeling and results 25

5.1 Model construction in Abaqus 25

5.1.1 Model with a uniform elastic layer 27

5.1.2 Model with an elastic and viscoelastic layer 28

5.1.3 Model with temperature dependent rheology . . . 35

6 Evaluation of the models 46

6.1 Model with an elastic and viscoelastic layer 46

6.2 Model with temperature dependent rheology 48

6.3 General discussion about the model results 51

7 Conclusions 54

A Physical background 60

A.1 Stress 61

A.2 Strain 63

A.3 Elasticity 65

A.4 Fluids 70

A.5 Viscoelasticity 72

B Finite element modeling **75**

B.1 Abaqus 75

C Values of parameter A **78**

List of Figures

1.1 Generalized figure of the formation of a graben 1
1.2 Map of the major tectonic plates 2
1.3 Fissure swarms and volcanic zones in Iceland 3
1.4 Photo over the area north of Thingvallavatn 5
2.1 Geological map over the WVZ 8
2.2 Map with faults in the WVZ 9
3.1 SPOT image over the study area including profile line, mapped lineaments and GPS sites 13
3.2 Topography north of Thingvallavatn from DEM and leveling line 15
3.3 Measured vertical displacements along leveling line north of Thingvallavatn 16
3.4 GPS measured spreading rates in the EVZ and the WVZ . 17
3.5 Measured cumulative widening north of Thingvallavatn . . 18
4.1 Schematic figure of three rheological models representing a divergent plate boundary 20
4.2 Sketch of cooling of oceanic lithosphere at a mid-ocean ridge 22
4.3 Temperature profiles from *Menke and Sparks* (1995) . . . 23
5.1 Appearance of the meshes used in the models 26
5.2 Applied boundary conditions on all finite element models 27
5.3 Subsidence for a uniform elastic thickness model 28
5.4 Subsidence for varying isotherms to define the layer boundary 30
5.5 Subsidence for varying thickness of the elastic thickness at the rift axis 31
5.6 Subsidence for varying viscosities of the viscoelastic material 31
5.7 Shear stress distribution for h_{axis} equal to 1 km 32
5.8 Shear stress distribution for h_{axis} equal to 3 km 33
5.9 Shear stress distribution for h_{axis} equal to 5 km 34
5.10 Thermal boundary conditions for the temperature dependent models 36
5.11 Calculated steady-state temperature distribution in the plate with high thermal gradient 37
5.12 Calculated steady-state temperature distribution in the plate with low thermal gradient 38
5.13 Values of the parameter A at different temperatures . . . 40

5.14 Subsidence result from the thermo-mechanical model . . . 42
5.15 Subsidence result for model C for varying spreading rates 43
5.16 Shear stress distribution in model C 44
5.17 Shear stress distribution in model C 45
A.1 Stress components that act on an infinitesimal cube 62
A.2 Displacement of the two particles P and Q to P' and Q' . 63
A.3 Sketch of an elastic plate with parameter explanations . . 68
A.4 The ratio of vertical and horizontal strain plotted versus Poisson's ration 69
A.5 Subsidence of an elastic plate as calculated in Abaqus . . 69
B.1 Overview of the different element types available in Abaqus 77

List of Tables

5.1 Specification of parameter values for the elastic-viscoelastic models . . . 29
5.2 Values of the parameters, put into Abaqus, for the power-law creep . . . 39
5.3 Calculated effective viscosities for model A, B and C . . . 41
C.1 Parameter values given in Abaqus for temperature dependent rheology model A . . . 78
C.2 Parameter values given in Abaqus for temperature dependent rheology model B . . . 78
C.3 Parameter values given in Abaqus for temperature dependent rheology model C . . . 79

Abbreviations used

EVZ	Eastern Volcanic Zone
GPS	Global Positioning System
MAR	Mid-Atlantic Ridge
NVZ	Northern Volcanic Zone
NUVEL	Global plate motion model by *DeMets et al.* (1990, 1994)
SPOT	Satellite Probatoire d'Observation de la Terre
WVZ	Western Volcanic Zone

Symbols and Constants

Symbol	Quantity	SI unit
a_i	acceleration	m s^{-2}
c	specific heat	J kg^{-1} K^{-1}
E	Young's modulus	Pa
h_{axis}	Elastic ridge axis thickness	m
H	activation energy	J mol^{-1}
k	thermal conductivity	W m^{-1} K^{-1}
K	bulk modulus	Pa
p	pressure	Pa
t	time	s
T	temperature	K
u_i	displacement	m
v_i	velocity	m s^{-1}
x_i	coordinate	m
X_i	body force	N m^{-3}
δ_{ij}	Kronecker delta	
ε	strain	
$\dot{\varepsilon}$	strain rate	s^{-1}
η	viscosity	Pa s
θ	cubical dilatation	
κ	thermal diffusivity	m^2 s^{-1}
λ	Lamé parameter	s^{-1}
μ	shear modulus	Pa
ν	Poisson's ratio	
ρ	density	kg m^{-3}
σ	stress	Pa
τ_M	relaxation time	s
Physical constants		
R	universal gas constant	8.31 J mol^{-1} K^{-1}

1 Introduction

The formation of graben structures at extensional rifts is the central part of this study and especially the role of plate movements. A graben is formed as the ground is stretched and part of it sinks down, as shown in Figure 1.1. Thingvellir in Iceland was used as a laboratory site to explore the process of graben formations. Thingvellir lies in the Western Volcanic Zone (WVZ) in Iceland and is part of the Mid-Atlantic Ridge (MAR), which marks the boundary between the North American plate and the Eurasian plate as seen in Figure 1.2.

The full spreading across southern Iceland is approximately 19 mm/yr in direction N104°E (*DeMets et al.*, 1990, 1994; *LaFemina et al.*, 2005; *Sigmundsson et al.*, 1995). However, in the southern part, the spreading is divided between two volcanic rift zones; the Western and the Eastern Volcanic Zone (EVZ). The structure of the spreading plate boundary is simpler in northern Iceland, where the Northern Volcanic Zone (NVZ) accommodates all the spreading (Figure 1.3).

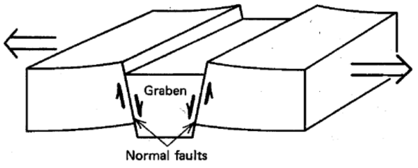

Figure 1.1: Generalized figure of the formation of a graben (*Turcotte and Schubert*, 2002).

GPS measurements in Iceland suggest that about 15–35 % of the spreading is accommodated by the WVZ, depending on latitude (*LaFemina et al.*, 2005). The measured spreading rate in the WVZ increases from northeast to southwest with the highest rate at Thingvellir; about 7 mm/yr (*LaFemina et al.*, 2005). The largest topographic relief is also found at Thingvellir with fault throws inside the inner part of the graben, that is covered by postglacial lavas, of about 30 m (*Guðmundsson*, 1987; *Sæmundsson*, 1992). These values can give an indication of the lower limit of cumulative vertical displacement in postglacial time, since faults outside Holocene lavas may have been displaced as well.

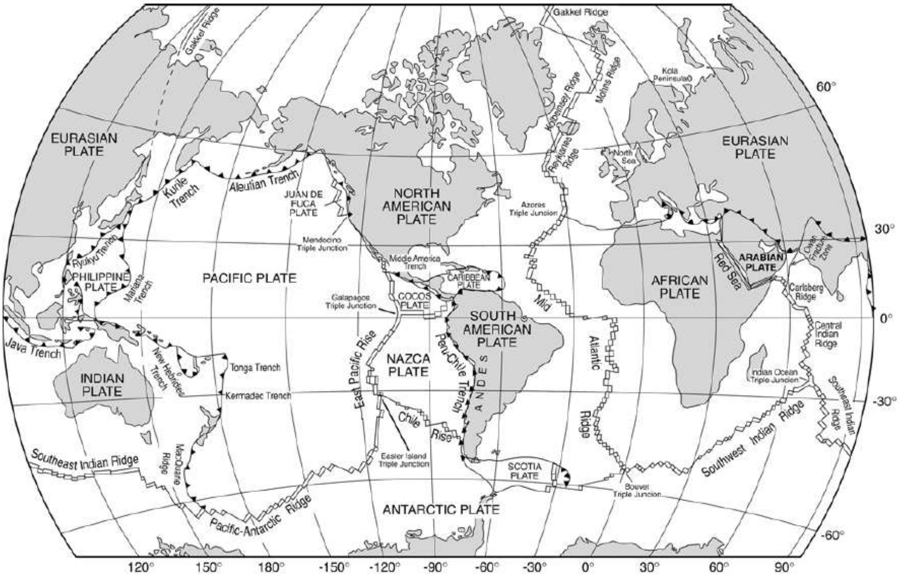

Figure 1.2: A map of the major tectonic plates with Iceland situated on the Mid-Atlantic Ridge. In the North Atlantic, it, marks the boundary between the North American plate and the Eurasian plate. In the South Atlantic, it marks the boundary between the South American plate and the African plate (*Fowler*, 2005).

As mentioned above, Iceland is the largest subaerial exposure of the MAR (*Sigmundsson*, 2006). It has been formed through excessive volcanic activity due to an interaction of a hotspot located at the site of Iceland and the MAR (*Sigmundsson*, 2006). Nevertheless, the erupted volume is small for the WVZ in postglacial time, except for the very early part of it (*Sinton et al.*, 2005). This study investigates if subsidence in the Thingvellir graben can to a large extent be a consequence of stretching across the plate boundary and the lack of magma infill. For this purpose a two-dimensional model was constructed in the Abaqus finite element package.

The constructed two-dimensional models were of an end-member type, in the sense that the models incorporated only stretching due to plate spreading; faulting and dike injections not considered although these processes may have been active as well. Three sets of models were tested

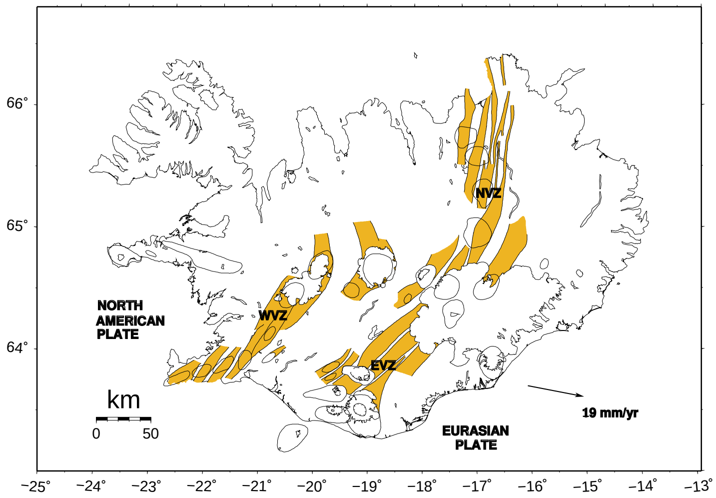

Figure 1.3: Fissures swarms (yellow color) and central volcanoes (oval outlines) in the volcanic zones of Iceland (*Einarsson and Sæmundsson*, 1987). The arrow shows the full spreading rate and direction estimated from the NUVEL-1A plate motion model (*DeMets et al.*, 1990, 1994) for southern Iceland.

with different layering and rheological properties. The first model was a pure elastic plate of uniform thickness. The second set of models consisted of two separate rheologic materials; an upper elastic layer and a lower viscoelastic layer. The geometry of the layer boundary between them was defined by an isotherm from the general equation of cooling of the oceanic lithosphere at spreading plate margins. For the third set of models, a temperature-dependent viscoelastic power-law creep was defined for the whole plate. A calculated steady-state temperature distribution in the plate was used as initial condition. The models were all subjected to a constant horizontal pull of 7 mm/yr over a distance of 20 km during 10 000 yrs which is about equivalent to the observed spreading rate at Thingvellir today.

1.1 Aim of the project

The aim of the project is to investigate if the amount of subsidence during postglacial time in the Thingvellir graben can be to a large degree the consequence of stretching of plates. It should be considered a study of an end-member model of the formation of Thingvellir graben where faulting and dikes are not incorporated. The finite element package Abaqus was used for the modeling. Topography and the amount of extension that has taken place in postglacial time served as constraints on the models, as well as leveling results.

Figure 1.4: Photo over the area north of Thingvallavatn with the large marginal fault Almannagjá seen as a sharp line on the left side of Lake Thingvallavatn. Photo by Ágúst Guðmundsson, GEOICE

2 Geological background

Iceland is a part of the Mid-Atlantic Ridge (MAR) that marks the boundary between the North American plate and the Eurasian plate (see Figure 1.2). It is the largest subaerial exposure of the mid-ocean ridge. The high topography around Iceland is the result of the interaction of the MAR and a hotspot (*Sigmundsson*, 2006). The MAR in southern Iceland has been formed through rift jumps and consists at present of two sub-parallel spreading centers, the Western Volcanic Zone (WVZ) and the Eastern Volcanic Zone (EVZ) (*Sigmundsson*, 2006).

About 6–7 Myrs ago the Snæfellsnes rift died out and spreading started further east, forming the WVZ (*Sæmundsson*, 1979). Another rift jump took place 1,5–3 Myrs ago when the rifting in the northern volcanic zone (NVZ) propagated southwards and the EVZ was created (*Sæmundsson*, 1979). Since then, spreading in south Iceland is divided between the WVZ and the EVZ (Figure 1.3). According to the NUVEL-1A plate motion model (*DeMets et al.*, 1990, 1994) the total amount of spreading across southern Iceland is 19 mm/yr directed N104°E. GPS measurements are consistent with this and they also indicate the mutual partitioning of spreading between the WVZ and the EVZ. Initial GPS measurements indicate that 85±15 % of the spreading was accommodated by the EVZ (*Sigmundsson et al.*, 1995) and the rest by the WVZ. Recent GPS measurements made by *LaFemina et al.* (2005) show that the spreading is latitude dependent and that the WVZ is among the slowest, volcanically active spreading rifts in the world, as the spreading rates are approximately 3–7 mm/yr. Within the zone, the highest rate of spreading is found near Thingvallavatn and further to the north it decreases.

Mapping done by *Bernauer* (1943) proposes a widening of 75 m of fractures at the surface during postglacial time and equivalent values are suggested by *Guðmundsson* (1987). If this is also representative for widening at depth, it yields an average spreading rate of 5–10 mm/yr for this period. Rift extension also causes continuous subsidence which is observed on leveling made since the 1960s on a profile across the Thingvellir graben just north of Thingvallavatn (*Tryggvason*, 1974; *Sigmundsson*, 2006). The observations show relative subsidence of about 1 mm/yr in the period 1966–1971, of the central part of the leveling line relative to its endpoints. The measurements give furthermore an exact estimate of the topographic relief.

The Thingvellir area can be divided into four volcanic systems, each with a fissure swarm related to a central volcano (*Sæmundsson*, 1978, 1992). Hengill central volcano together with the Thingvellir fissure swarm constitutes the main system. East of Hengill lies the Hrómundartindur system that is located along the east shore of Lake Thingvallavatn. Prestahnjúkur central volcano is located in the southwest part of Langjökull with an associated fissure swarm that extends along the northwestern margin of the rift zone. The fourth volcanic system that has been defined by *Sæmundsson* (1978) is the system with Kálfstindar as the probable central volcano with fissures reaching northwards towards Langjökull. Geology of the area is shown in Figure 2.1.

2.1 Eruptive history

The eruptive history of the WVZ in postglacial time is concentrated in the first 3000 yrs after deglaciation, when almost 64 % of the total erupted volume was produced (*Sinton et al.*, 2005). Decompression of the mantle as the ice melted away is inferred to be the cause of the large amount of melt. *Sinton et al.* (2005) estimated the total erupted volume of the WVZ in postglacial time to be about 40 km^3. It can be compared with the total erupted volume in the EVZ during postglacial time that is estimated to be 200 km^3 (*Jakobsson*, 1979). Shield lavas make up the majority of lavas in the WVZ and *Sinton et al.* (2005) showed that only about 4 % of the erupted volume originate from fissures. The fissure eruptions are mostly located south of Lake Thingvallavatn in the Hengill and Hrómundartindur systems (*Sæmundsson*, 1992).

The most recent rifting event in the WVZ occurred in 1789 in the Hengill volcanic system, but no lava was erupted (*Sæmundsson*, 1992). The movements in this event showed clearly that the fissures of Thingvellir belong to the Hengill volcanic system as offsets of 1–2 m are imposed on faults north of Lake Thingvallavatn (*Sæmundsson*, 1992).

The most recent eruption was about 1900 yrs ago and it formed Nes-

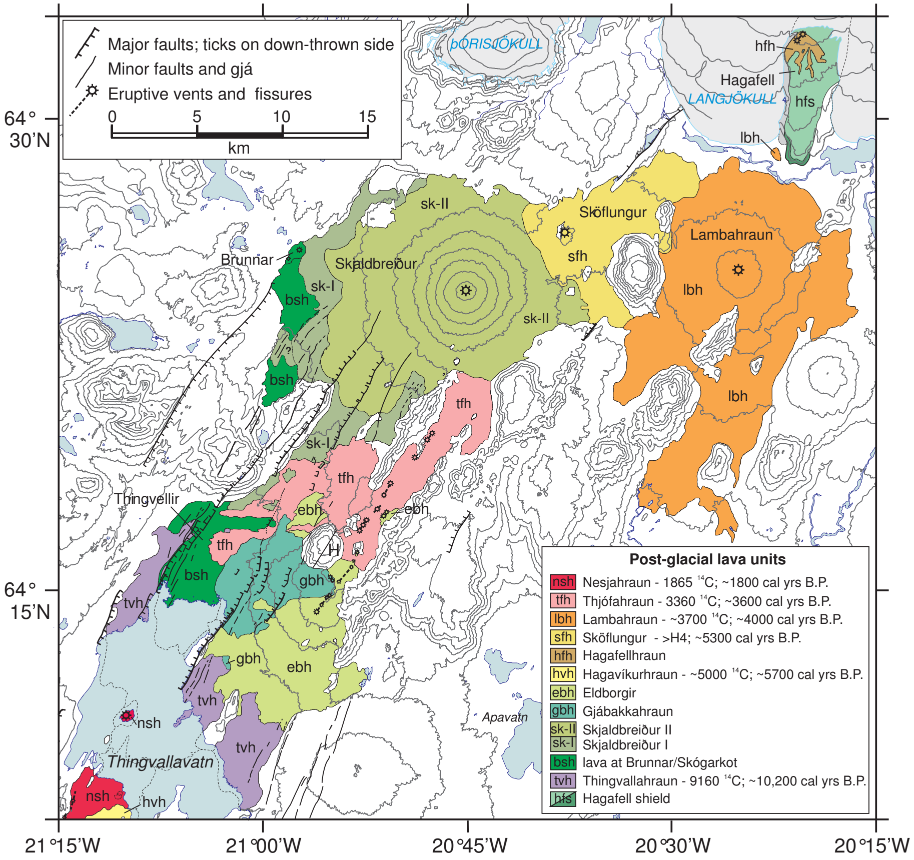

Figure 2.1: Geological map from *Sinton et al.* (2005) showing postglacial lavas around Lake Thingvallavatn. Major faults mapped by *Sæmundsson* (1992) are also showed.

jahraun, a lava field, that flowed out of a fissure south of Thingvallavatn and continued northward into the lake (Figure 2.1). Associated with this eruption is also the formation of the tuff cone of Sandey that is located in the middle of Lake Thingvallavatn (*Sæmundsson*, 1992).

2.2 Thingvellir graben

The combination of small erupted volume, except for the very early postglacial time, and continuous extension in the WVZ has created a deep graben structure, with the largest topographic relief at Lake Thingvallavatn. An eastward shift of the eruptive centers north of Thing-

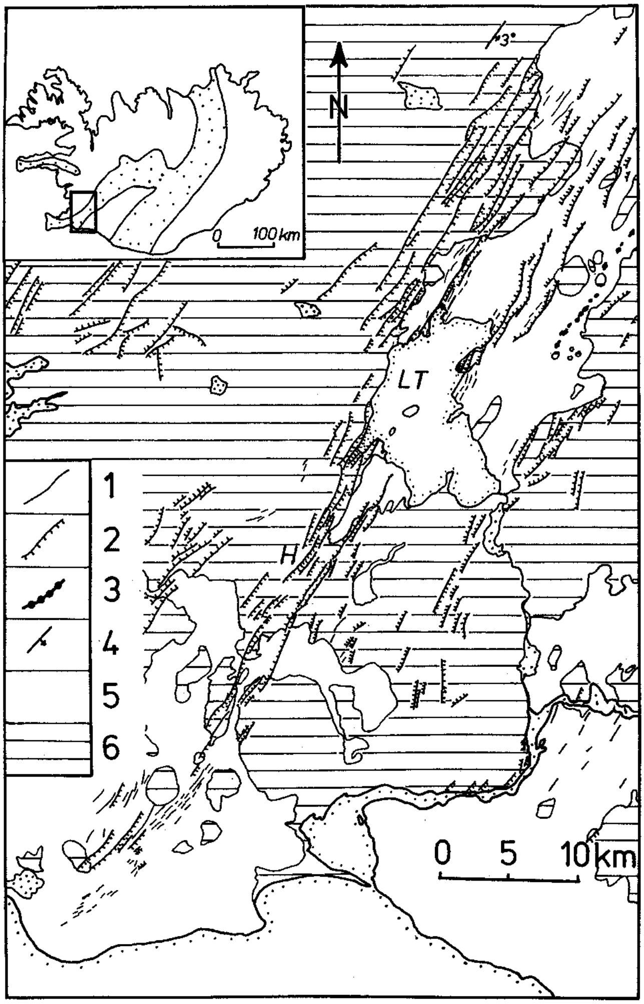

Figure 2.2: Fault map from *Guðmundsson* (1987). LT stands for Lake Thingvallavatn, 1 – tectonic fissure, 2 – normal fault, 3 – volcanic fissure, 4 – strike and dip, 5 – Holocene lavas and 6 – Pleistocene rocks.

vallavatn appears also to have contributed to the formation of the graben (*Sinton et al.*, 2005).

The depression around Thingvallavatn which forms the graben structure is 20–25 km wide in the northeast and narrows to about 10 km in the southwest (*Sæmundsson*, 1992). The major trend of faults and fissures in the rift zone is N30°E (*Sæmundsson*, 1992; *Guðmundsson*, 1987). *Sæmundsson* (1992) observed in his study that the throw of faults seems to be proportional to the age of the lava/rock that they cut through. The largest throw he detected was 400 m and located northwest of Lake Thingvallavatn, formed in rock that probably date from the third last glaciation (about 200 000 yrs ago). For faults in younger rocks and lavas, the throw decreases. Almannagjá and Hrafnagjá have the largest vertical displacements for faults in postglacial lava with throws of about 30 m (*Sæmundsson*, 1992; *Guðmundsson*, 1987).

The graben is asymmetric and *Sæmundsson* (1992) describes the geometry of the graben as follows; In the northwest the faults are situated closely together and they have large throws. To the east, the faults have less vertical offsets and are spread out through central and eastern parts of the graben. The western marginal faults, with Almannagjá as the largest, have an east dip and the faults at the eastern margin, with Hrafnagjá as the largest, have a dip to the west.

2.3 Lake Thingvallavatn

The Almannagjá and Hrafnagjá marginal faults continue into Lake Thingvallavatn (*Thors*, 1992). Interpretation of reflection seismic and sonograph surveys made by *Thors* (1992) in Lake Thingvallavatn show that these two large faults pass over into others faults in the southwest. In particular he noted that the amount of faults increase significantly to the SW and also their throw. The deepest part of Thingvallavatn is west of Sandey and it reaches a depth of more than 100 m, 13 m below sea level (*Sæmundsson*, 1992). The average depth is 40–80 m. The largest fault throws in the lake are found north of Sandey. On the western marginal fault about 55 m and on the segmented eastern part up to 40 m (*Bull et al.*, 2003).

The floor of Lake Thingvallavatn has been inferred to be made of two postglacial lava flows, hyaloclastite material and sediments. The northern and eastern parts of the lake are covered with the approximately 10.2 kyrs old Thingvallahraun (see Figure 2.1) that forms a steep edge as it ends (*Kjartansson*, 1964; *Sinton et al.*, 2005). *Bull et al.* (2003) suggests that the large flow of Thingvallahraun to the east is an indication that the deepest part of the lake was further to the east in early postglacial time than it is today. The Nesjahraun aged 1.89±0.06 kyrs has flowed out into the southern part of the lake and formed a gently sloping plane (*Sæmundsson*, 1992). This lava is not cut by any faults (*Thors*, 1992) which suggests that no movements have occurred on the northern fissures of Hrómundartindur system during the last 2 kyrs. In the western and southeastern parts of Thingvallavatn the lake bed consists of hyaloclastite material that has not been covered by postglacial lava (*Thors*, 1992). Sediments are found everywhere in the lake where the water depth is more than a few meters and uneven distribution of sedimentation is found along profiles examined by *Thors* (1992) and *Bull et al.* (2003). *Haflidason et al.* (1992) concludes from his experiments that sedimentation rate increases proportional to water depth in water deeper than 30 m. *Bull et al.* (2003) uses this statement to conclude that the major western fault must have moved recently since the sediments are thickest away from the presently deepest part, which is next to the western fault.

3 Crustal deformation and faulting

The previous chapter described the geology of the WVZ, and especially the area around Thingvellir. This chapter is a compilation of horizontal and vertical deformation data from the Thingvellir area that provide constraints for the finite element models.

An overview of the study area is shown in Figure 3.1. Indicated lineaments, such as faults and fissures, were mapped in ArcGIS from a set of SPOT images and are divided into two groups; lineaments within postglacial lavas and those outside, in older rocks. The average strike of fractures in the Thingvellir area is suggested to be about N30°E from earlier studies (*Sæmundsson*, 1992; *Guðmundsson*, 1987). The mapping of lineaments in this study also resulted in a strike direction of approximately N30°E. Figure 3.1 also shows the location of the leveling line measured by *Tryggvason* (1974) as well an extended profile line that shows the cross-section for the two-dimensional models produced for this study. GPS sites used in deformation studies examined by *LaFemina et al.* (2005) are also shown. The horizontal displacements from *LaFemina et al.* (2005) and measurements of widening of fractures in the graben give constraints on horizontal movements. The topography and the vertical displacement rate measured from the leveling line, together with throw estimates on the major marginal faults Almannagjá and Hrafnagjá done by *Guðmundsson* (1987), constitute the vertical data constraints on the models. The throws of Almannagjá and Hrafnagjá, respectively, mark the lower limit of subsidence in postglacial time. It is difficult to say how large displacements have occurred in postglacial time on faults away from the central part of the graben, since these faults cut through rocks that are not postglacial.

As mentioned above, all fault studies in the Thingvellir area give an average strike direction around N30°E. The estimated spreading direction from the NUVEL-1A plate motion model (*DeMets et al.*, 1990, 1994) is N104°E. In this study, to enable the assumption of plane strain in the modeling, a plate spreading direction perpendicular to the average strike of faults is assumed. This assumption gives a spreading direction of N120°E.

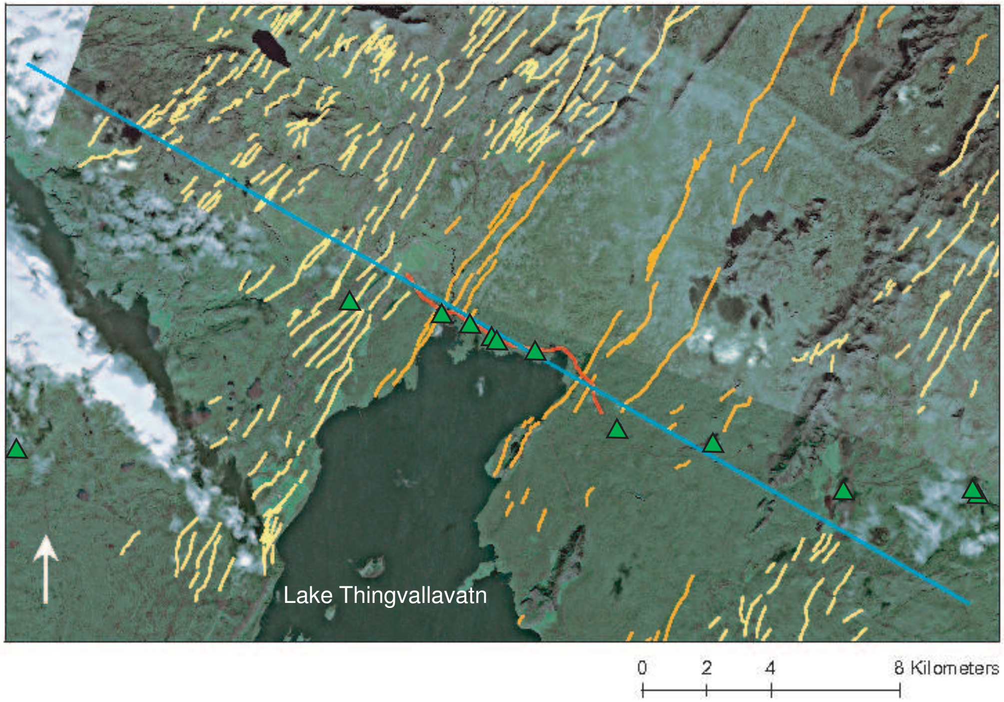

Figure 3.1: SPOT image over Thingvellir with faults within (orange lines) and outside (yellow lines) of postglacial lavas. The leveling line measured by *Tryggvason* (1974) is marked with red color and the extended profile line that defines the cross-section for the 2D models is marked with a blue line. Green triangles represent GPS sites measured by *LaFemina et al.* (2005)

3.1 Constraints on vertical displacements

Tryggvason (1974) presents data from a survey of a leveling line along the northern shore of Thingvallavatn (see Figure 3.1 for location). The initial data span from 1966 to 1971, and these give a detailed topographic profile of the Thingvellir graben north of the lake as well as vertical displacement velocity in these years (Figure 3.2). The leveling line is centered around the central rift axis and extends less than 4 km to the east and west, respectively. The deformation zone in the WVZ appears to be about 20 km wide at this location (*LaFemina et al.*, 2005; *Sigmundsson*, 2006). The topography for the whole width of the deformation zone was found from a digital elevation model (DEM). The DEM had a grid space of 20 by 20 m and was made from 20 m contour lines from a 1:50 000 map database from the Land Survey of Iceland (*Ólafsdóttir* (2007), personal communication). The topography of the DEM is smoother than the real topography because of the interpolation between grid points. Nevertheless, the sharp throws of the marginal faults are still visible, as seen in Figure 3.2(a).

Vertical displacements from 1966 to 1971 are about 1 mm/yr (*Tryggvason*, 1974), in the center of the graben (Figure 3.3). However, this value is relative to the endpoint of the leveling line that is less than 4 km away from the central axis. The subsidence rate relative to a point further away from the ridge axis, that is not part of the deformation zone, would probably give larger vertical velocities.

Throws on Almannagjá and Hrafnagjá have been measured by *Guðmundsson* (1987). The throw varies along the faults but as an average the throw on Almannagjá is about 15 m and about 8 m on Hrafnagjá. Maximum throw is approximately 30 m (*Guðmundsson*, 1987; *Sæmundsson*, 1992). Since the faults cut through 9–10 kyrs old lava flows, the displacement on Almannagjá and Hrafnagjá has certainly taken place in postglacial time. A lower limit of 30 m of subsidence in Thingvellir graben during postglacial time can hence be estimated from the throws of the marginal faults.

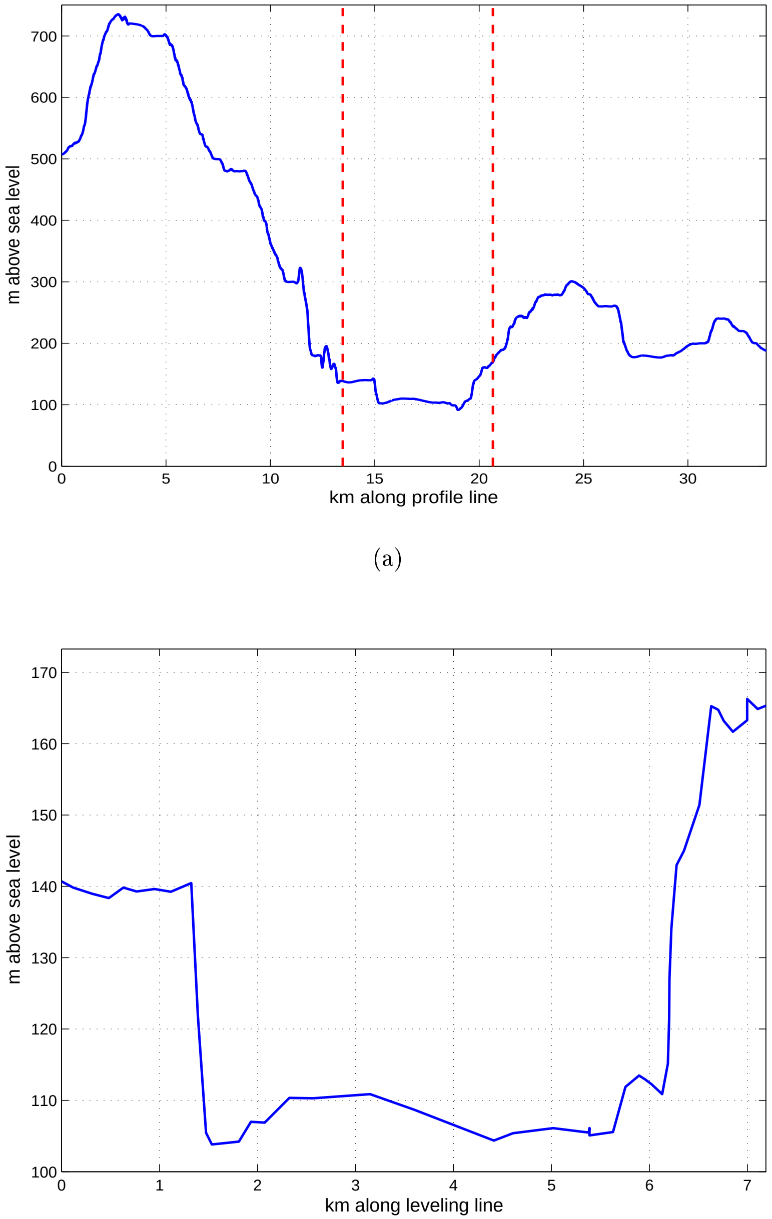

(b)

Figure 3.2: (a) Topography along the extended profile line that defines the cross-section for the models in this study. The height data is extracted along the profile line from the DEM. The dashed red lines indicate the section that coincides with the stretch of the leveling line. (b) Results from the leveling line measured by *Tryggvason* (1974). See Figure 3.1 for the location of the extended profile line and the leveling line.

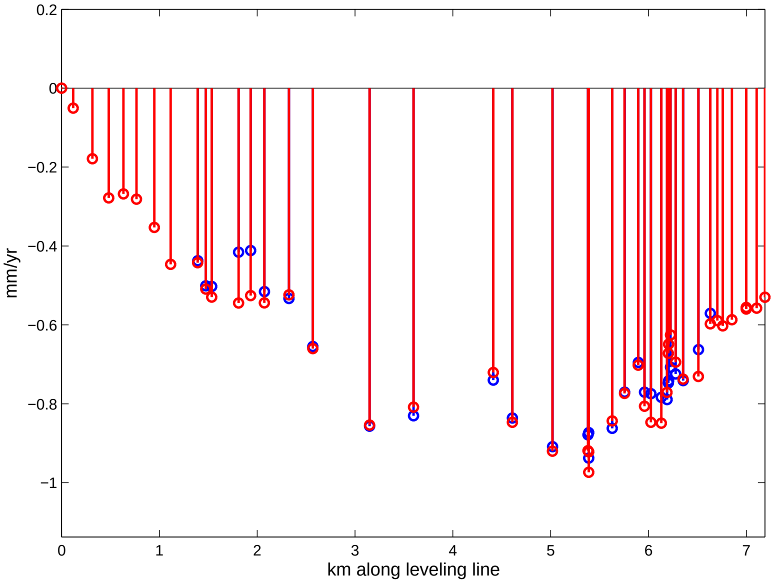

Figure 3.3: Vertical displacement rate from 1966–1971 (blue) and 1967–1971 (red) as measured by *Tryggvason* (1974).

3.2 Constraints on horizontal displacements

In the work of *LaFemina et al.* (2005), spreading velocities for the WVZ are suggested to be about 7 mm/yr at the latitude of Thingvellir (Figure 3.4(a) and (b)). There is an observed along strike variation of the spreading velocity along the WVZ, with lowest values to the northeast and increasing velocities to the southwest. The highest values are estimated around lake Thingvallavatn. Widening of fractures can also give an estimate of the extension during postglacial time. *Guðmundsson* (1987) measured the widening of Almannagjá and Hrafnagjá along their whole extension. The widening varies significantly with distance along the faults. An approximate average widening of the two faults applicable to the location of the profile line is 30 m.

As a supplement to the measurements done by *Guðmundsson* (1987), the opening of seven smaller fractures inside the graben were measured in this study with a tape measure. The cumulative extension of these

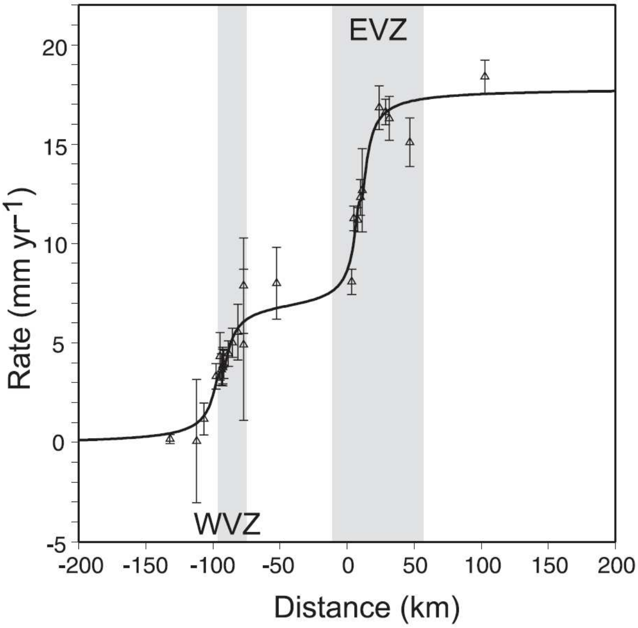

(a)

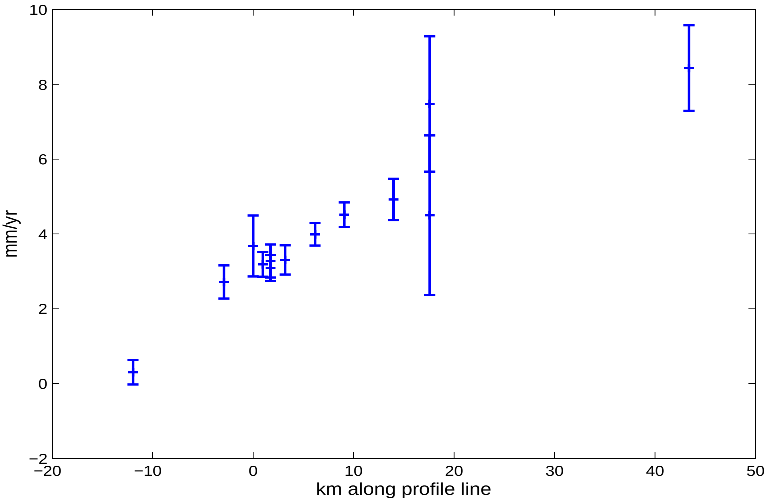

(b)

Figure 3.4: (a) Measured spreading rates for the WVZ and the EVZ relative to stable North America (*LaFemina et al.*, 2005). The horizontal velocities are projected on to the direction N102°E. The solid line indicates the best fit result from modeling done by (*LaFemina et al.*, 2005). (b) The same GPS data as in (a), but only for the WVZ and projected on to the direction N120°E, the direction of the profile line in this study.

fissures were approximately 45 m. Together with the measured widening by *Guðmundsson* (1987) the total extension in postglacial time for the Thingvellir graben is approximately 105 m (Figure 3.5), but the uncertainties are large.

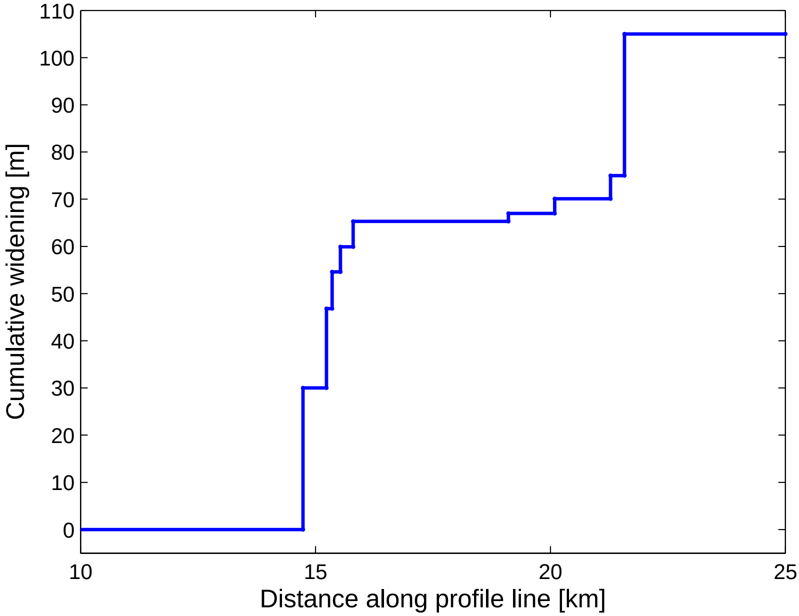

Figure 3.5: The cumulative widening of the two marginal faults Almannagjá and Hrafnagjá (*Guðmundsson*, 1987) and seven smaller fractures inside Thingvellir graben measured in this study. The estimated values of opening of Almannagjá and Hrafnagjá are an average value from the measurements by (*Guðmundsson*, 1987). The measurements of the seven smaller fractures were all done near the profile line, just north of Lake Thingvallavatn.

It is not well known how the surface extension reflects the extension at deeper level. Open surface fractures have typically walls of large rotated blocks so that the fractures are closed at depth. The measurements of widening across open surface fractures will therefore give an overestimate of the extension in postglacial time. However, it can be used to give an indication of the spreading velocity in postglacial time. The measured cumulative opening of 115 m in 10 000 yrs gives a spreading rate of 10.5 mm/yr. This is comparable with the GPS derived spreading rate of 7 mm/yr from *LaFemina et al.* (2005). In this study, the spreading rate of 7 mm/yr from *LaFemina et al.* (2005) has been used as horizontal constraint for the cross-sectional models.

4 Rheological models of a divergent plate boundary

The rheology of the Earth varies with depth. Deformation of the upper parts of the crust with low confining pressure and temperature can be described by elasticity, but for the lower parts, the Earth properties are better described by viscoelastic behavior (*Sigmundsson*, 2006). Figure 4.1 shows three rheological models that represent the appearance of a divergent plate boundary with depth.

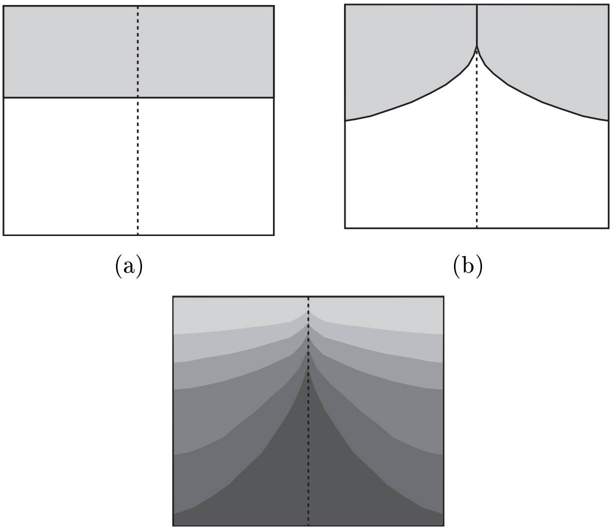

(a) (b)

(c)

Figure 4.1: Schematic figure of three different rheological models that could represent a divergent plate boundary. Dotted line marks the central axis of the plate boundary. (a) The most simplified case with an upper elastic layer of uniform thickness above a viscoelastic material. (b) An elastic upper layer on top of a viscoelastic layer. The boundary is defined by a given isotherm from the general equation of cooling of oceanic lithosphere, with an additional correction for non-zero elastic thickness at the ridge axis. (c) The model has no boundaries instead it is prescribed a viscoelastic rheology that depends on temperature.

4.1 Uniform elastic thickness

Figure 4.1(a) shows a commonly used model setup used in e.g. modeling of glacial rebound data (e.g. *Pagli et al.* (2007)). This model may be oversimplified for detailed modeling of deformation of a divergent plate boundary, since only uniformly subsidence will occur if the plate is only stretched, and not loaded vertically. An analytical solution is derived for the vertical subsidence in a pure elastic plate in Appendix A, Chapter A.3. The result is compared to what is computed in Abaqus for the same model setup. The results are in accordance and confirm that the subsidence is uniform over the whole surface.

4.2 Curved elastic-viscoelastic boundary

Figure 4.1(b) shows a model with a curved boundary between an elastic and a viscoelastic layer. The shape of this boundary is assumed to follow the general cooling plate model of oceanic lithosphere at divergent plate boundaries (Figure 4.2). This model gives the temperature distribution in the oceanic lithosphere around mid-ocean ridges as the solution of the heat conduction problem of sudden cooling of a half-space (*Turcotte and Schubert*, 2002). A constant temperature is assumed at the ridge axis, throughout its whole depth. In this solution, only vertical heat conduction is considered and the plates are assumed to spread apart with a constant horizontal velocity. Hot mantle material rises at the ridge axis and starts to cool when it reaches the surface. As the hot material moves away from the ridge axis the cooling continues down from the surface and the depth to a given isotherm can be written as (*Turcotte and Schubert*, 2002)

$$h = 2\mathrm{erf}^{-1}\Big(\frac{T - T_0}{T_1 - T_0}\Big)\sqrt{\frac{\kappa x_1}{v_1}} \tag{4.1}$$

where erf^{-1} is the inverse error function, T_0 is the temperature at the surface, T_1 is the temperature at the ridge, T is the temperature of the given isotherm, κ is the thermal diffusivity, x_1 is the coordinate axis defined to coincide with the spreading direction, v_1 is the spreading velocity and h is the depth for the given isotherm T.

Laboratory experiments on the behavior of olivine which is the major mineral in the upper mantle show that the response on applied stress varies significantly with temperature. At temperatures less than about 675°C dry olivine deforms elastically and the corresponding limit for wet olivine is 475°C (*Turcotte and Schubert*, 2002). Dry and wet olivine corresponds to water free and water saturated olivine ($\sim$ 0.03 wt %),

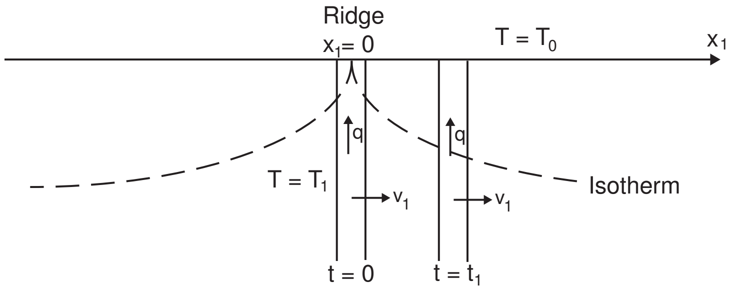

Figure 4.2: Sketch of cooling of oceanic lithosphere at a mid-ocean ridge from *Turcotte and Schubert* (2002), where q is the vertical heat conduction, v_1 is the spreading velocity, t is time, T_0 is the surface temperature and T_1 is the ridge axis temperature

respectively (*Karato and Wu*, 1993). For higher temperatures olivine acts as a fluid and flows. The depths of the 475°C and 675°C isotherms in oceanic lithosphere can give a rough estimate on the thickness of the elastic part in a plate.

The cooling plate model predicts zero thickness of the elastic layer at the ridge axis which is not in accordance with what is observed at the subaerial exposure of the MAR in Iceland. Circulation of water in fractures provides an explanation of this discrepancy, as well as discrete diking events at the ridge axis. For the models presented here, an extra term h_{axis} has been added to Equation 4.1 to correct for this discrepancy, ensuring a non-zero elastic layer thickness also at the ridge axis.

4.3 Temperature dependent rheology

The third model, Figure 4.1(c), shows a plate without boundaries but with a temperature dependent viscoelastic rheology. This thermo-mechanical model is assigned a calculated initial temperature distribution in the plate with a constant surface temperature and a depth dependent ridge axis temperature. The temperature gradient in the upper crust in Iceland varies widely, from almost 0 to 500°C/km (*Flóvenz and Sæmundsson*, 1993). Away from the volcanic zones, in older rock, the temperature gradients are typically about 40-50°C/km and in the flank zones of the active volcanic zones, the temperature rises up to about 150-200°C/km (*Pálmason and Sæmundsson*, 1979; *Flóvenz and Sæmundsson*, 1993). Interpretations of results regarding the thermal structure of Iceland have given two separate models; the thin-crust and the thick-crust model. The thin-crust model assumes a crustal thickness of 10-15 km with a layer of partially molten basalt at the base of about 1100°C (*Pálmason and Sæmundsson*, 1979; *Flóvenz and Sæmundsson*, 1993; *Björnsson*, 2007). On the other hand, the thick-crust model which assumes a relatively cold crust with a thickness of up to 40 km (*Sigmundsson*, 2006; *Kaban et al.*, 2002; *Menke et al.*, 1995; *Menke and Sparks*, 1995). The thick-crust model is based on results from seismic data, both new and reinterpreted old data (*Bjarnason, I. Th. and Menke, W. and Flóvenz, Ó. and Caress, D.*, 1993; *Menke et al.*, 1995; *Menke and Sparks*, 1995; *Kaban et al.*, 2002). This study relies on the interpretations from the new seismic data, favoring the thick-crust model.

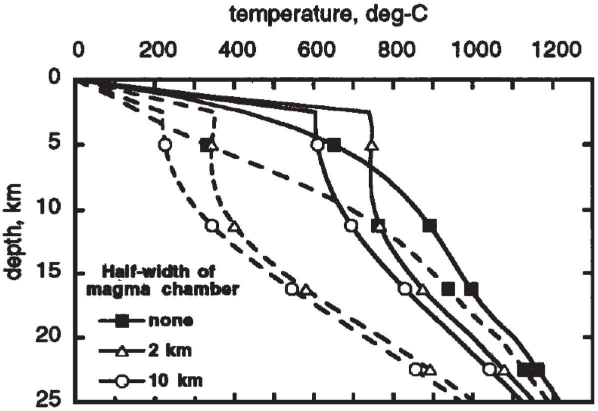

Figure 4.3: Model results from *Menke et al.* (1995) for temperature at depth in the Icelandic crust. The dashed and solid lines indicate models where hydrothermal circulation is taken into account and not, respectively. The half-width values of a magma chamber refers to the model setup in the modeling done by *Menke and Sparks* (1995)

The rheological law of the lower crust and upper mantle can be determined from laboratory experiments on olivine. These show that the relation between strain rate and stress depends strongly on pressure and temperature (*Karato and Wu*, 1993; *Turcotte and Schubert*, 2002). The experiments suggest a non-Newtonian (see Appendix A, Chapter A.4) dependency between strain rate and stress, described as (*Kirby and Kronenberg*, 1987; *Ranalli*, 1995; *Tsenn and Carter*, 1987; *Turcotte and Schubert*, 2002; *Watts*, 2001)

$$\dot{\varepsilon} = A_p e^{-H/RT} \sigma^n \tag{4.2}$$

where A_p is a material-specific parameter, σ is the differential stress $\sigma_{11} - \sigma_{33}$, n gives the power-law dependence of strain rate to stress, H is the activation energy, R is the universal gas constant, and T is the temperature in Kelvin. Experiments on olivine done by *Goetze* (1978) estimated strain rate to have a cubic dependence to stress, i.e. $n = 3$. *Karato et al.* (1986) suggested $n = 3.5$ for dry olivine and $n = 3$ for wet, as do *Turcotte and Schubert* (2002). The activation energy H and the material specific parameter A_p also differs depending on wet or dry conditions of olivine, see Chapter 5.1.3 for suggested values.

Because of limitations in the laboratory equipment, all experiments have been made at lower pressure and with higher strain rates than what is present in the Earth. Equation 4.2 and the related estimated values of n, A_p and H are assumed to be valid also when extrapolated to pressures and strain rates according to the conditions in the lower crust and mantle (*Watts*, 2001; *Turcotte and Schubert*, 2002).

The viscosity of non-Newtonian fluids can be defined in the same way as for Newtonian fluids. If normal stress and strain rates are used, the definition is (*Turcotte and Schubert*, 2002; *Ranalli*, 1995)

$$\eta = \frac{\sigma}{3\dot{\varepsilon}} \tag{4.3}$$

When the empirical determined power-law in Equation 4.2 is inserted into the above definition of viscosity, this gives a stress dependent viscosity called the effective viscosity written as (*Ranalli*, 1995; *Turcotte and Schubert*, 2002)

$$\eta_{eff} = \frac{e^{H/RT}}{3A_p} \sigma^{1-n} \tag{4.4}$$

5 Finite element modeling and results

5.1 Model construction in Abaqus

The modeling was performed in two dimensions and symmetry about the spreading ridge was assumed to be valid for all the models. Thus, all models had the ridge axis as boundary on one side and the width was one half of the interpreted deformation zone width. Figure 5.2 displays the geometry of the models.

A shell structure with unit thickness was utilized to construct the models in Abaqus. Figure B.1 shows the appearance of a shell element. The first models utilized a mesh with 3 node triangular elements, named CPE3. The coupled thermo-mechanical models utilized a mesh consisting of 4-node quadrilateral elements, named CPE4T. Both types of mesh have two degrees of freedom; horizontal and vertical translation. The size of the elements were 100 m near the upper left corner, along the surface and along the boundaries between the layers and became more sparse towards the base and to the right. Both types of meshes are showed in Figure 5.1. *Wu* (2004) discusses the use of commercial finite element packages as Abaqus for the use of solving stress and strain problems applied to the Earth. In Abaqus the equations of motions are set to equal zero so the calculations are done for a non-self gravitating plate without any isostasy force.

All models had the same boundary conditions as displayed in Figure 5.2. At the ridge axis, the left side of the model, only vertical displacement was allowed. The right side relating to the intraplate boundary (the boundary inside the tectonic plate) was free to move vertically and was displaced 35 m horizontally in 10 000 yrs corresponding to GPS derived spreading rates (*LaFemina et al.*, 2005; *Sigmundsson et al.*, 1995). The base of the model was restricted to move only horizontally. No boundary conditions were applied to the surface. The applied boundary condition to the right of 35 m stretching in 10 000 yrs was given as a constant pull of 3.5 mm/yr.

The width of the models, that is assumed to represent the half width of the deformation zone in the WVZ, was determined according to GPS data from *LaFemina et al.* (2005), where an approximately 20 km wide

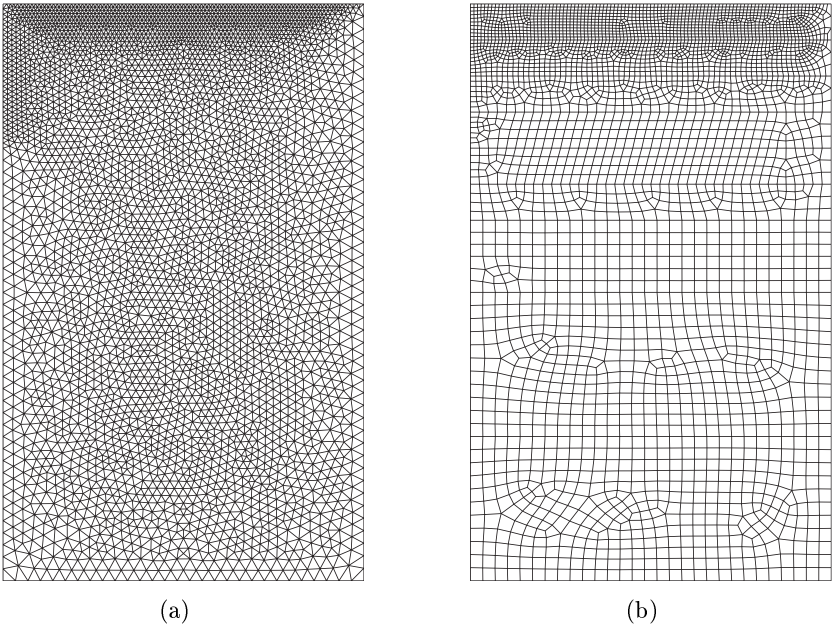

Figure 5.1: (a) Mesh with triangular elements (b) Mesh with quadrilateral elements.

deformation zone north of Thingvallavatn is suggested. This gives a model width of 10 km if symmetry of the graben is assumed. The depth of all models is 16 km. It was determined from the deepest of the boundary isotherm in the elastic-viscoelastic models. In this way all models, also the ones with a higher temperature isotherm as boundary layer between the elastic and viscoelastic layer, had a viscoelastic layer at the bottom. For consistency this depth was kept for all models. The determination of the depth of the models and its consequences, are further discussed in Chapter 6.3.

This information as well as the geometry of the models was put together in a script. The script was written in the object oriented programming language Python and was read into Abaqus.

The resulting vertical displacement from the models were all analyzed as relative displacement, meaning that the subsidence at the intraplate boundary was subtracted from the results. This assumption is discussed in Chapter 6.3.

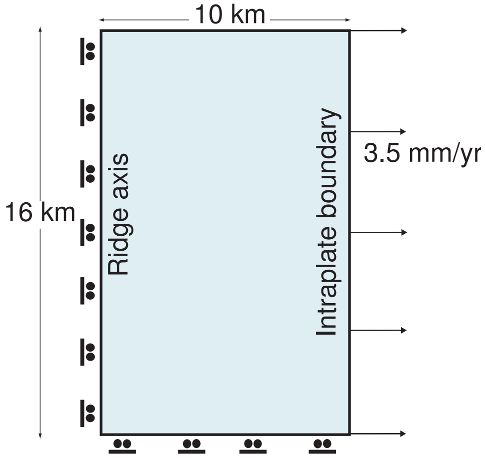

Figure 5.2: Mechanical boundary conditions applied to all models. The ridge axis is fixed horizontally but free to move vertically, the base is fixed vertically but free to move horizontally. The surface is free to move in any direction and the intraplate boundary is stretched 35 m in 10 000 yrs.

5.1.1 Model with a uniform elastic layer

A uniform elastic layer on top of a viscoelastic material comprises the first model. The thickness of the elastic layer can be estimated from e.g. the depth distribution of earthquakes. A compilation of focal depths in south Iceland show that the they range from a maximum of about 7 km depth in the west to a few kilometers deeper in the east (*Stefánsson et al.*, 1993). Seismic data can also be used to approximate the elastic thickness. From seismic data and examination of temperature gradients in Hengill geothermal area *Foulger* (1995) prescribes a seismogenic layer of maximum 6–7 km depth around Hengill. *Kaban et al.* (2002) comes up with a similar result from gravity and seismic data and propose an elastic plate thickness for Iceland of maximum 6 km.

To sum up; the elastic thickness beneath southwestern Iceland is estimated to have an average of 7 km but seems to thicken away from the ridge axis. For this model, an elastic thickness of 7 km was used.

The elastic layer had Young's modulus $E = 75$ GPa and Poisson's ratio

$\nu = 0.25$ and the elastic properties of the viscoelastic layer were set to $E = 90$ GPa and $\nu = 0.25$ (*Turcotte and Schubert*, 2002; *Watts*, 2001). The elastic parameter values were all according to estimated values of oceanic lithosphere. The parameters for the viscous properties described by Equation B.1 were set to $n = 1$, $m = 0$ and $A = 1/3\eta$. The vertical displacement at the surface is shown in Figure 5.3 and is explained and discussed in Chapter 6.

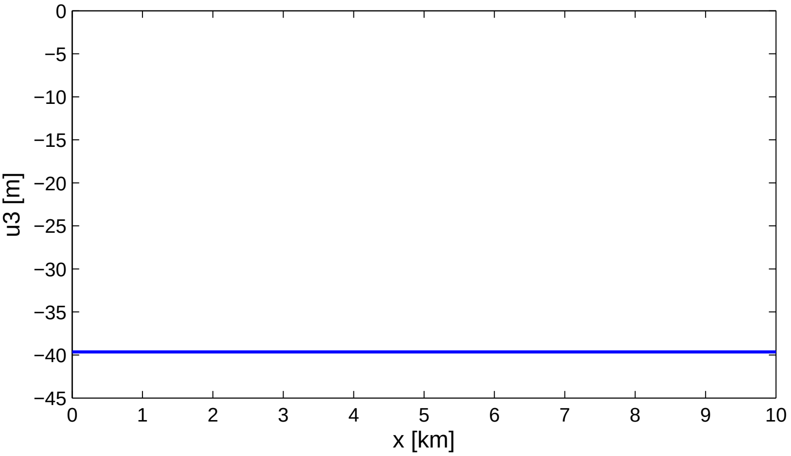

Figure 5.3: Subsidence for the model with a layer of uniform elastic thickness above a viscoelastic material. The subsidence is uniform over the entire model surface and in contrast to all other vertical displacement results showed in this chapter, this is the total subsidence for the model.

The resulting stress distribution for this model is uniform throughout the elastic and viscoelastic layer, respectively, with higher values of stress in the elastic layer. The horizontal normal stress σ_{11} (in the direction of stretching) is 280 MPa in the elastic layer and 0.18 MPa in the viscoelastic layer. The horizontal normal stress σ_{22} (perpendicular to the direction of stretching) is 70 MPa and 0.18 MPa for the elastic and the viscoelastic layer, respectively. The vertical normal stress σ_{33}, as well as the shear stress σ_{13}, are both zero throughout the whole model.

5.1.2 Model with an elastic and viscoelastic layer

This model was constructed with an elastic top layer and a Maxwell viscoelastic layer beneath. The boundary geometry between the elastic and the viscoelastic layer was assumed to have the shape of a given isotherm from the cooling of oceanic lithosphere at spreading ridges proposed in *Turcotte and Schubert* (2002) (see Chapter 4.2), with the addition of an elastic plate thickness h_{axis} at the ridge axis. This cooling model, with the modification of an extra h_{axis} gives the depth of a given isotherm versus distance from rift center as (see Chapter 4.2)

$$h = 2\mathrm{erf}^{-1}\Big(\frac{T - T_0}{T_1 - T_0}\Big)\sqrt{\frac{\kappa x_1}{v_1}} + h_{axis} \tag{5.1}$$

where the parameters were set to; surface temperature $T_0 = 20°\mathrm{C}$, ridge axis temperature $T_1 = 1100°\mathrm{C}$ (*Turcotte and Schubert*, 2002), thermal diffusivity $\kappa = 10^{-6}$ m^2 s^{-1} (*Turcotte and Schubert*, 2002) and $v_1 = 3.5$ mm yr^{-1} (*LaFemina et al.*, 2005). The temperature T of the isotherm corresponding to the change of elastic to viscoelastic behavior, was varied between 400 and 700°C to test the subsidence response of different isotherms. The elastic layer thickness at the ridge axis and the viscosity of the Maxwell viscoelastic layer were also altered to investigate their mutual effect on vertical subsidence. The different model setups are shown in Table 5.1.

Varied isotherm	Varied axis thickness	Varied viscosity
T = 400 – 700°C	T = 500°C	T = 500°C
$\eta = 8{\cdot}10^{18}$ Pa s	$\eta = 8{\cdot}10^{18}$ Pa s	$\eta = 1{\cdot}10^{18} - 1{\cdot}10^{20}$ Pa s
$h_{axis} = 3000$ m	$h_{axis} = 500 - 5000$ m	$h_{axis} = 3000$ m

Table 5.1: Specification of the parameter values used in the different models for the elastic-viscoelastic models.

The elastic layer had Young's modulus $E = 75$ GPa and Poisson's ratio $\nu = 0.25$ and the elastic properties of the viscoelastic layer were set to $E = 90$ GPa and $\nu = 0.25$ (*Turcotte and Schubert*, 2002; *Watts*, 2001). The elastic parameter values were all according to estimated values of oceanic lithosphere. The parameters for the viscous properties described by Equation B.1 were set to $n = 1$, $m = 0$ and $A = 1/3\eta$. The results from the different model setups are shown in Figures 5.4, 5.5 and 5.6 respectively. The results are explained and discussed in Chapter 6.

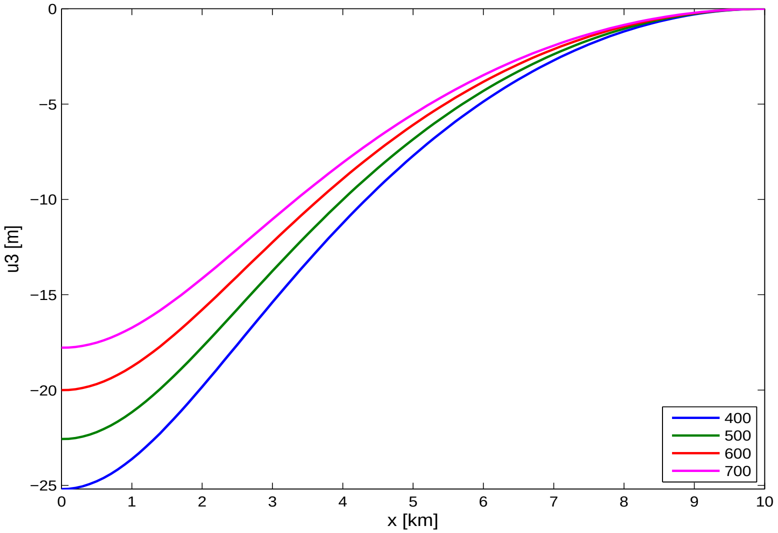

Figure 5.4: Subsidence for isotherms between 400 and 700°C. The isotherms defined the boundary between elastic and viscoelastic behavior in the model.

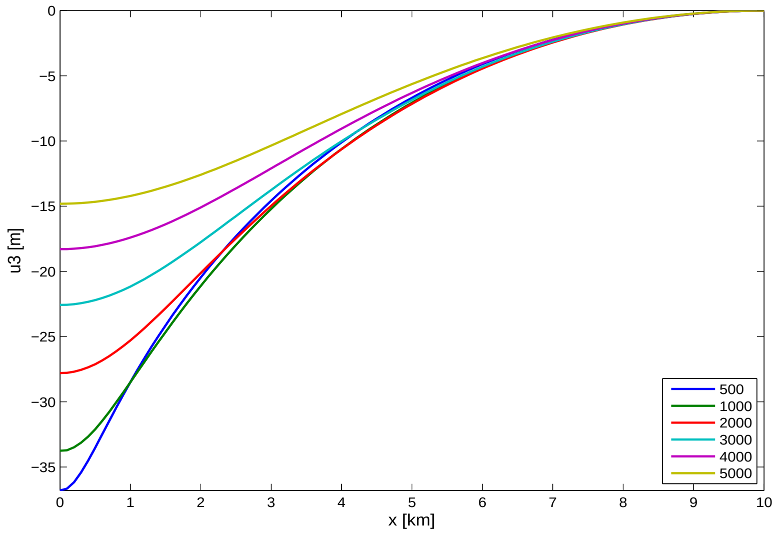

Figure 5.5: Subsidence for varying thickness of the elastic thickness at the ridge axis. The thickness was varied from 500 m to 5000 m.

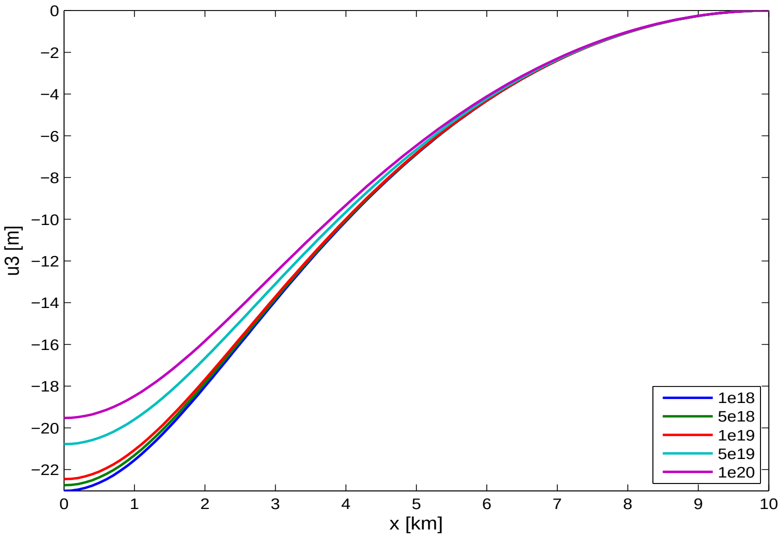

Figure 5.6: Subsidence for varying viscosities of the viscoelastic material. The smallest value of the viscosity was $1{\cdot}10^{18}$ Pa s and the largest tested was $1{\cdot}10^{20}$ Pa s.

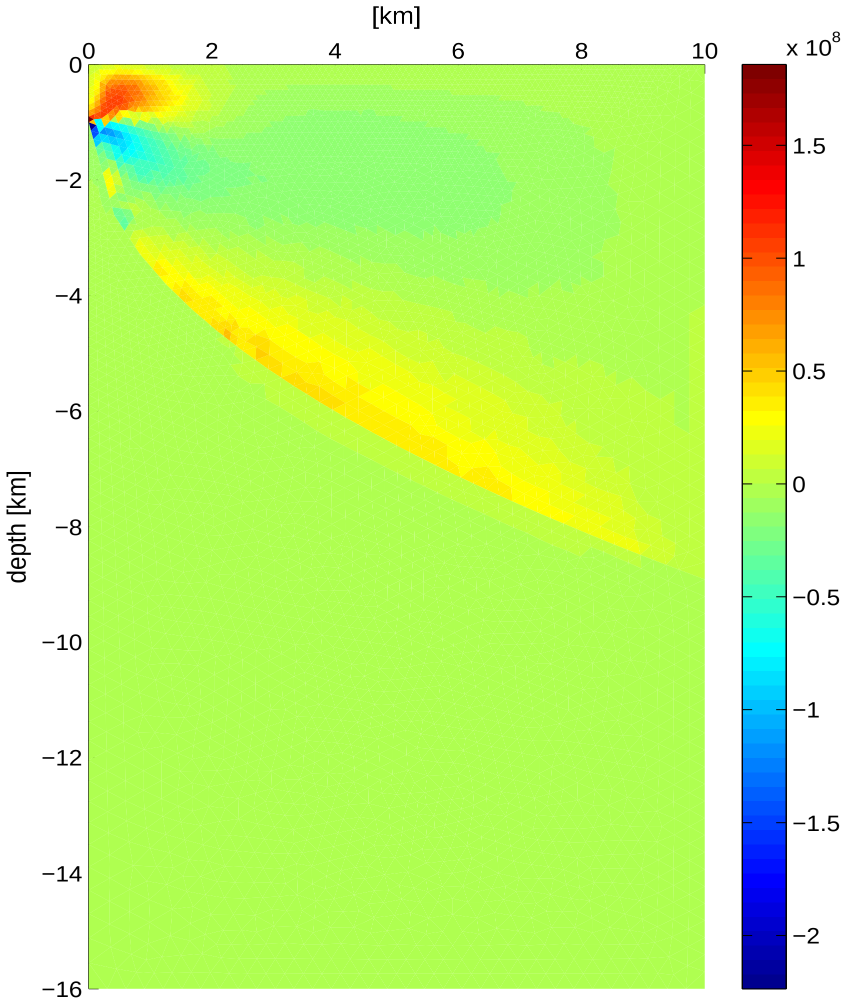

Figure 5.7: Shear stress σ_{13} distribution in a model with a 1 km thick elastic layer at the ridge axis. See Table 5.1 for other model parameters. The stress values are given in Pa.

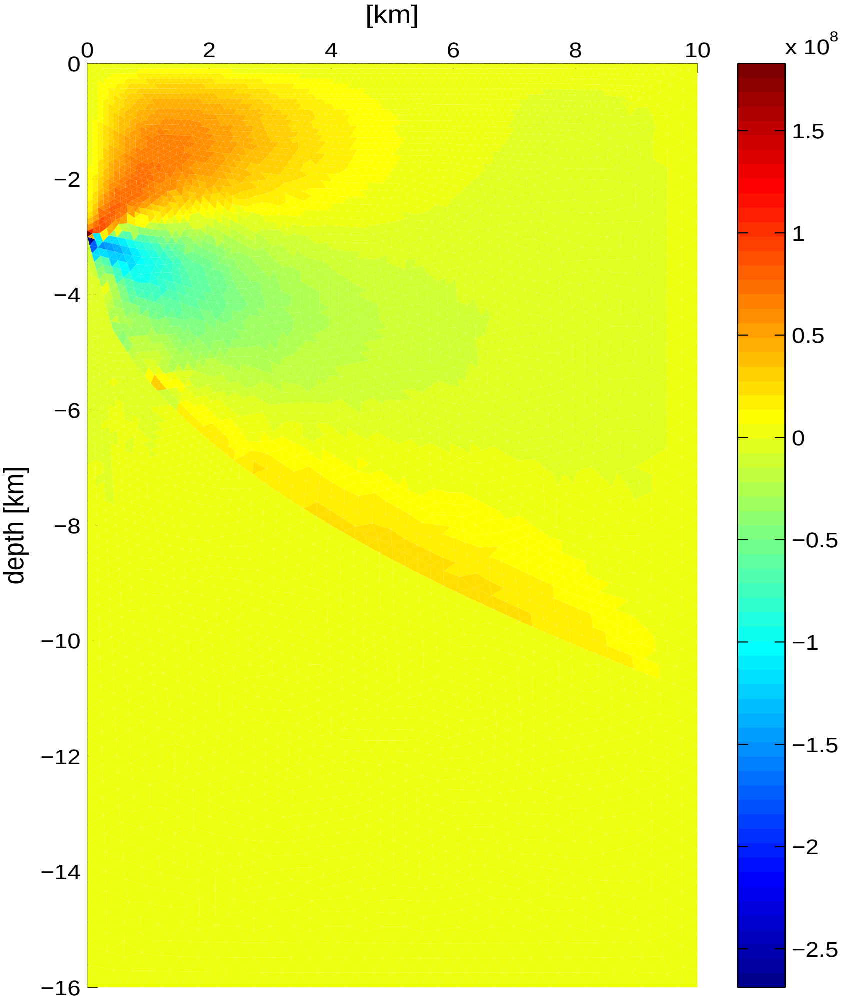

Figure 5.8: Shear stress σ_{13} distribution in a model with a 3 km thick elastic layer at the ridge axis. See Table 5.1 for other model parameters. The stress values are given in Pa.

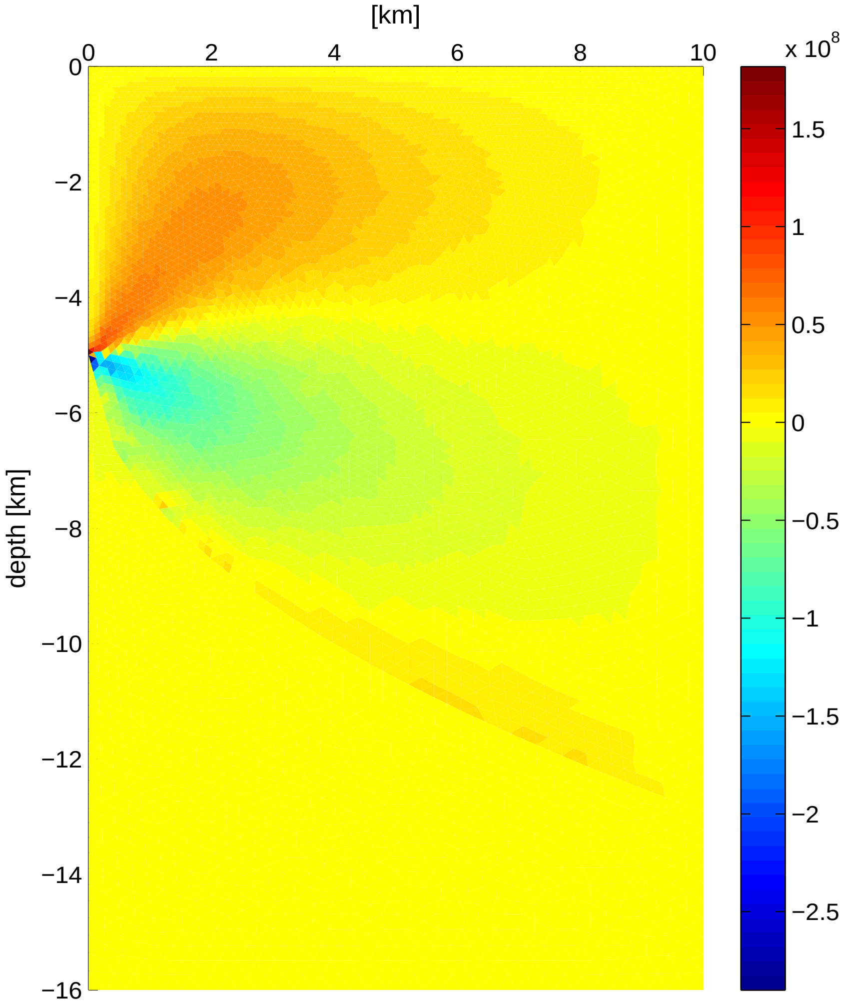

Figure 5.9: Shear stress σ_{13} distribution in a model with a 5 km thick elastic layer at the ridge axis. See Table 5.1 for other model parameters. The stress values are given in Pa.

Stress distribution

The model results showed a focusing of shear stress σ_{13} (x_1 is parallel to the spreading direction and x_3 is the vertical direction), starting at the elastic-viscoelastic boundary at the ridge axis and spreading diagonal upwards. Figure 5.7, 5.8 and 5.9 show the shear stress distribution for the models with $h_{axis} = 1, 3, 5$ km, respectively. The distance from the ridge axis to the surface location of the focusing, was strongly dependent on the elastic ridge axis thickness h_{axis}. As h_{axis} was increased, the distance from ridge axis to the stress focusing also increased.

5.1.3 Model with temperature dependent rheology

In the third set of models, a steady-state temperature distribution was used as initial condition and a temperature-dependent creep-law was set as constitutive equation. Two types of thermal boundary conditions were used to calculate the temperature distribution and for each of these two calculated temperature distributions, three different empirical creep-law rheologies were tested.

The two types of thermal boundary conditions were both according to the "thick-crust model" (see Chapter 4.3) with a relatively cold crust under Iceland (*Menke et al.*, 1995; *Menke and Sparks*, 1995; *Kaban et al.*, 2002; *Sigmundsson*, 2006). The surface temperature was 20°C. The base and the intraplate boundary did not have any thermal boundary conditions. The ridge axis was assigned different temperature gradients. All thermal boundary conditions are showed in Figure 5.10. Figure 5.11 and 5.12 show the two calculated steady-state temperature distributions resulting from these thermal boundary conditions.

The model was designed in two steps. In the first step, thermal boundary conditions, as mentioned above, were applied and the steady-state temperature distribution was calculated for the model within Abaqus. In the second step, these results were used as initial condition and the mechanical boundary conditions, as shown in Figure 5.2, were applied.

The rheology of the models were determined by the empirical power-law creep given in Equation 4.2. When the empirical rheologic equation is compared with the creep-law given in Abaqus, Equation B.1, it is seen

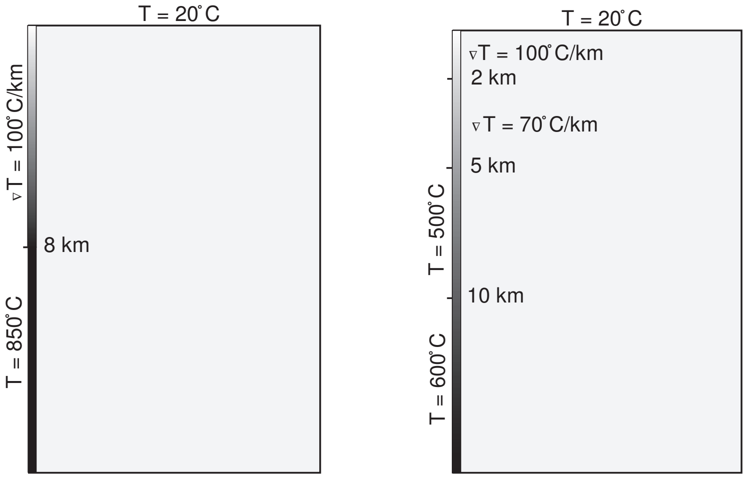

(a) (b)

Figure 5.10: (a) Thermal boundary conditions for temperature distribution I. The temperature gradient $\partial T/\partial x_3$ (x_3 is the vertical coordinate) at the ridge axis is 100°C/km during the first 8 km and thereafter is a constant temperature of 850°C defined at the axis (b) Thermal boundary conditions for temperature distribution II. The ridge axis temperature gradient $\partial T/\partial x_3$ is 100°C/km during the first 2 km, ∇T = 70°C/km between 2 and 5 km depth, thereafter is the temperature constant at 500°C from 5 to 10 km and at 600°C from 10 to 16 km depth.

that the value of the parameter A that needs to be inserted into Abaqus can be written as

$$A = A_p e^{-H/RT} \tag{5.2}$$

where R is the universal gas constant, T is temperature in Kelvin and the parameter A_p and the activation energy H are empirically determined. Three models were created; model A, B and C, corresponding to empirically determined values of A_p and H as shown in Table 5.2. Table 5.2 also show all other parameter values that were needed for the modeling. The values of $A = A_p e^{-H/RT}$ that were inserted into Abaqus are shown in Figure 5.13 and are also listed in Appendix C.

The smallest value Abaqus can handle is 10^{-27} (*Abaqus*, 2007). As seen in Figure 5.13, the values of A include values smaller than this limit at temperatures less than 200-400°C depending on model. All values that are smaller than 10^{-27}, are set to $5\cdot10^{-27}$ Pa^{-3}yr^{-1}. The units of pa-

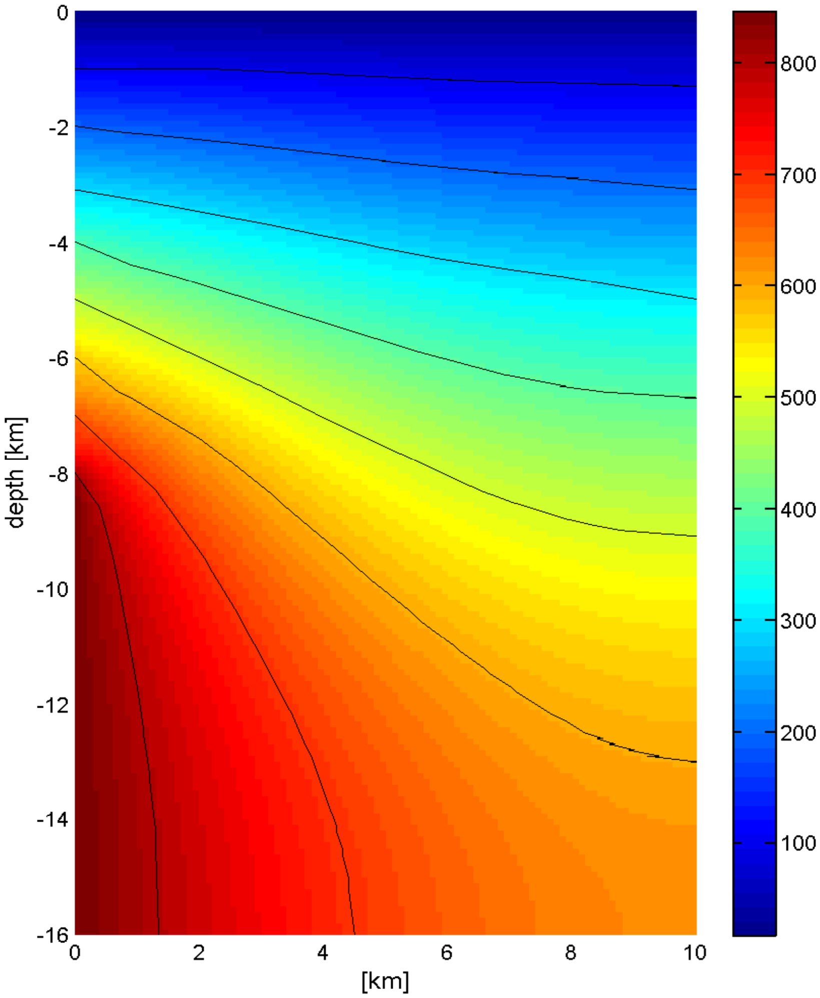

Figure 5.11: Temperature distribution I. Calculated steady-state temperature distribution in the plate with a constant surface temperature of 20°C, a temperature gradient of 100°C/km during the upper 8 km and below that a constant temperature of 850°C at the ridge axis. The base and the intraplate boundary were not prescribed any boundary conditions. The temperatures are showed in °C and the black lines indicate every 100°C isotherm.

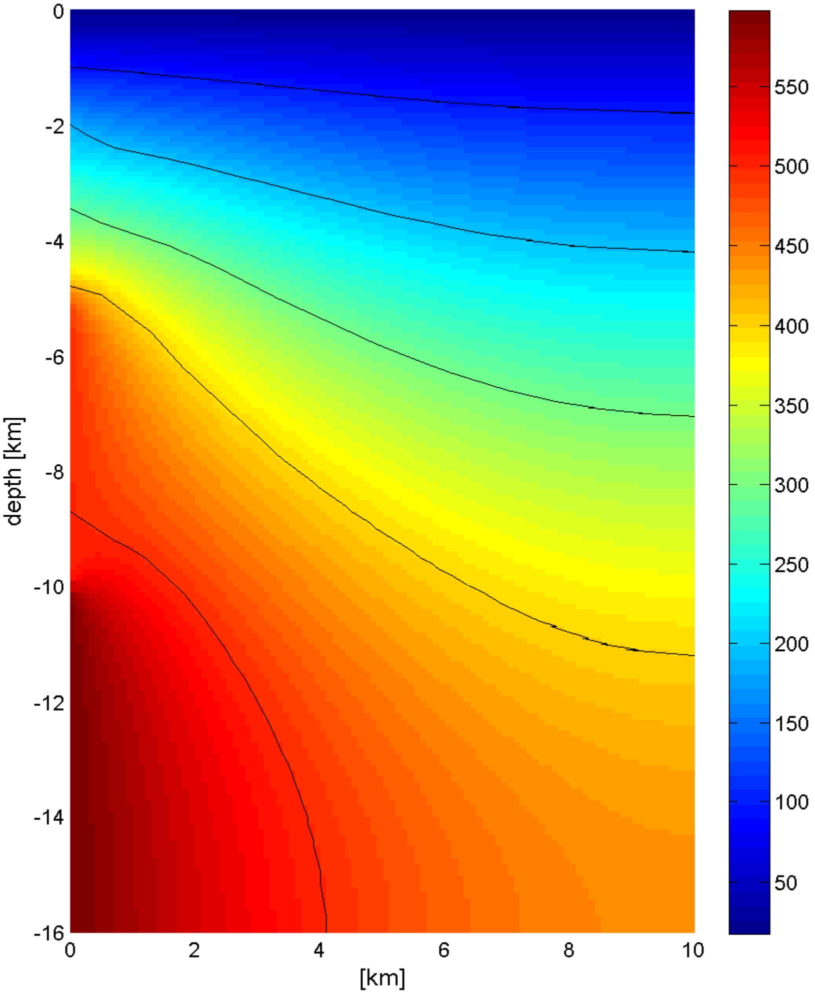

Figure 5.12: Temperature distribution II. Calculated steady-state temperature distribution in the plate with a constant surface temperature of 20°C The ridge axis had a temperature gradient of 100°C/km during the first 2 km. Between 2 and 5 km, the temperature gradient was 70°C/km and thereafter was the temperature constant at 500°C until 10 km depth and below that constant at 600°C. The base and the intraplate boundary were not prescribed any boundary conditions. The temperatures are showed in °C and the black lines indicate every 100°C isotherm.

	Model A	Model B	Model C
A_p [$\mathrm{Pa}^{-3}\mathrm{yr}^{-1}$]	$1.73{\cdot}10^{18}$	$1.32{\cdot}10^{19}$	$2.15{\cdot}10^{13}$
H [$\mathrm{kJ\ mol}^{-1}$]	398	520	520

Parameters equal for all models

n	3
specific heat c_p	1000 J $\mathrm{kg}^{-1}\mathrm{K}^{-1}$
thermal conductivity k	1.8 W $\mathrm{m}^{-1}\mathrm{K}^{-1}$
density ρ	2900 kg m^{-3}
Young's modulus E	90 GPa
Poisson's ratio ν	0.25

Table 5.2: The values of A_p and H for model A are from *Turcotte and Schubert* (2002) and correspond to wet olivine. Model B and C have values according to dry olivine, with A_p and H from *Turcotte and Schubert* (2002) and *Kirby* (1983), respectively. All models are assigned a cubical relation between stress and strain rate. The remaining parameter values, correspond to typical material parameters for basalt taken from *Turcotte and Schubert* (2002); *Fowler* (2005); *Flóvenz and Sæmundsson* (1993)

rameter A could also have been changed to e.g. MPa $^{-3}\mathrm{yr}^{-1}$ instead of $\mathrm{Pa}^{-3}\mathrm{yr}^{-1}$ to increase the values of A (this of course affects other parameters, and they would need to be changed as well to retain consistency of units). However, since the values of A are already given in $\mathrm{Pa}^{-3}\mathrm{yr}^{-1}$ and not $\mathrm{Pa}^{-3}\mathrm{s}^{-1}$, a value of $5{\cdot}10^{-27}$ $\mathrm{Pa}^{-3}\mathrm{yr}^{-1}$ will result in strain rates equivalent to those found in the elastic layer in the earlier models. The resulting elastic strain rates for these models were $10^{-13} - 10^{-14}$ s^{-1}. The creep-law behavior described in Equation 4.2 results in a strain rate of about 10^{-13} s^{-1}, with $A = 5{\cdot}10^{-27}$ $\mathrm{Pa}^{-3}\mathrm{yr}^{-1}$ and a differential stress σ of 10 MPa. This simplification of cutting off the values of A will be discussed further in Chapter 6.2.

Figure 5.14(a) and 5.14(b) show the subsidence for model A, B and C. For the results in Figure 5.14(a), the temperature distribution I (Figure 5.11) is used as initial condition, with a maximum ridge temperature of 850°C. For the results in Figure 5.14(b), the temperature distribution

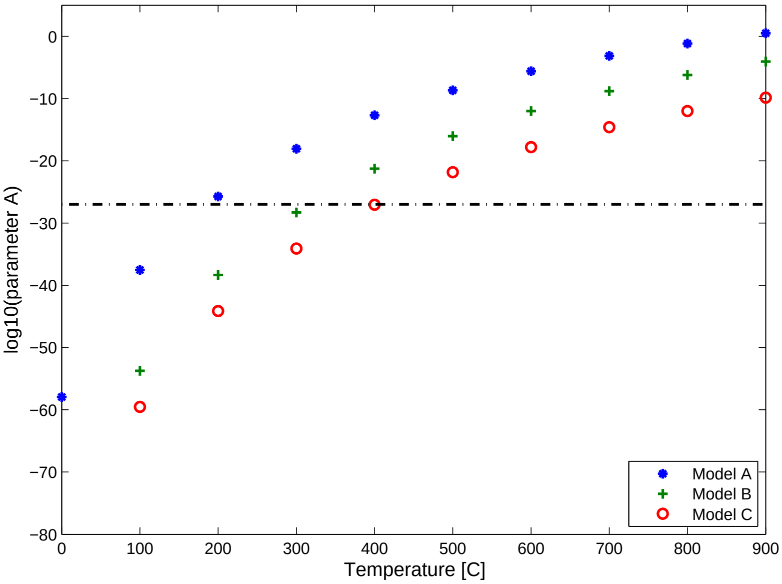

Figure 5.13: Plotted values of the base-10 logarithm of parameter A for model A, B and C described in Table 5.2. The exact values of A are listed in Appendix C. The dashed line indicate the lower limit of values that Abaqus can handle; 10^{-27} (*Abaqus*, 2007).

II (Figure 5.12) is used as initial condition, with a maximum ridge temperature of 600°C.

The spreading rate was also varied to see the effect on the resulting subsidence. This was performed for model C and the modeled vertical displacements are shown in Figure 5.15 for spreading rates of 3, 7, 10 and 14 mm/yr.

For the models with an elastic upper layer and a lower Newtonian viscoelastic layer, the viscosity of the viscoelastic layer was inserted into the Abaqus parameter A as $A = 1/3\eta$, see Chapter A.4 and Chapter B.1. The temperature dependent rheology models have non-Newtonian properties which introduces a stress dependence for the viscosity, or effective viscosity as it is called for non-Newtonian fluids, as described in Chapter A.4. The effective viscosity at different temperatures for model A, B and C, can be inferred by using the definition of effective viscosity for normal stress and strain rate, written as (*Ranalli*, 1995)

$$\eta_{eff} = \frac{e^{H/RT}}{3A_p}\sigma^{1-n} \tag{5.3}$$

where R is the universal gas constant, T is temperature in Kelvin and values of A_p and H are taken from *Turcotte and Schubert* (2002) and *Kirby* (1983). Representative values of $\sigma = \sigma_{11} - \sigma_{33}$ at different temperatures were taken from the model results of stress.

The resulting values of the effective viscosity η_{eff}, in Pa s, are shown in Table 5.3.

$\Delta T[°C]$	Model A	Model B	Model C
150-200	$3.2{\cdot}10^{22}$	$5.0{\cdot}10^{35}$	$2.9{\cdot}10^{41}$
200-250	$3.4{\cdot}10^{22}$	$4.2{\cdot}10^{29}$	$2.2{\cdot}10^{35}$
250-300	$2.7{\cdot}10^{19}$	$9.6{\cdot}10^{24}$	$3.2{\cdot}10^{23}$
300-350	$1.9{\cdot}10^{19}$	$3.1{\cdot}10^{23}$	$3.0{\cdot}10^{26}$
350-400	$1.2{\cdot}10^{17}$	$3.8{\cdot}10^{20}$	$1.6{\cdot}10^{23}$
400-450	$1.4{\cdot}10^{17}$	$2.8{\cdot}10^{20}$	$4.8{\cdot}10^{22}$
450-500	$3.5{\cdot}10^{15}$	$2.6{\cdot}10^{18}$	$3.4{\cdot}10^{20}$
500-550	$8.9{\cdot}10^{15}$	$5.5{\cdot}10^{18}$	$5.7{\cdot}10^{20}$
550-600	$9.5{\cdot}10^{14}$	$4.8{\cdot}10^{17}$	$6.0{\cdot}10^{19}$
600-650	$6.2{\cdot}10^{13}$	$2.0{\cdot}10^{16}$	$1.8{\cdot}10^{18}$
650-700	$1.0{\cdot}10^{13}$	$1.2{\cdot}10^{15}$	$1.0{\cdot}10^{17}$
700-750	$1.4{\cdot}10^{13}$	$2.1{\cdot}10^{15}$	$1.6{\cdot}10^{17}$
750-800	$3.7{\cdot}10^{12}$	$3.2{\cdot}10^{14}$	$3.1{\cdot}10^{16}$
800-850	$1.4{\cdot}10^{12}$	$1.5{\cdot}10^{14}$	$1.5{\cdot}10^{16}$

Table 5.3: Calculated effective viscosity values for models A, B and C, respectively. The values are given in Pa s. Earlier studies of viscosity below Iceland indicate a viscosity of about $4\text{–}10{\cdot}10^{18}$ Pa s (*Pagli et al.*, 2007) and $\sim 10^{19} - 10^{20}$ Pa s (*LaFemina et al.*, 2005)

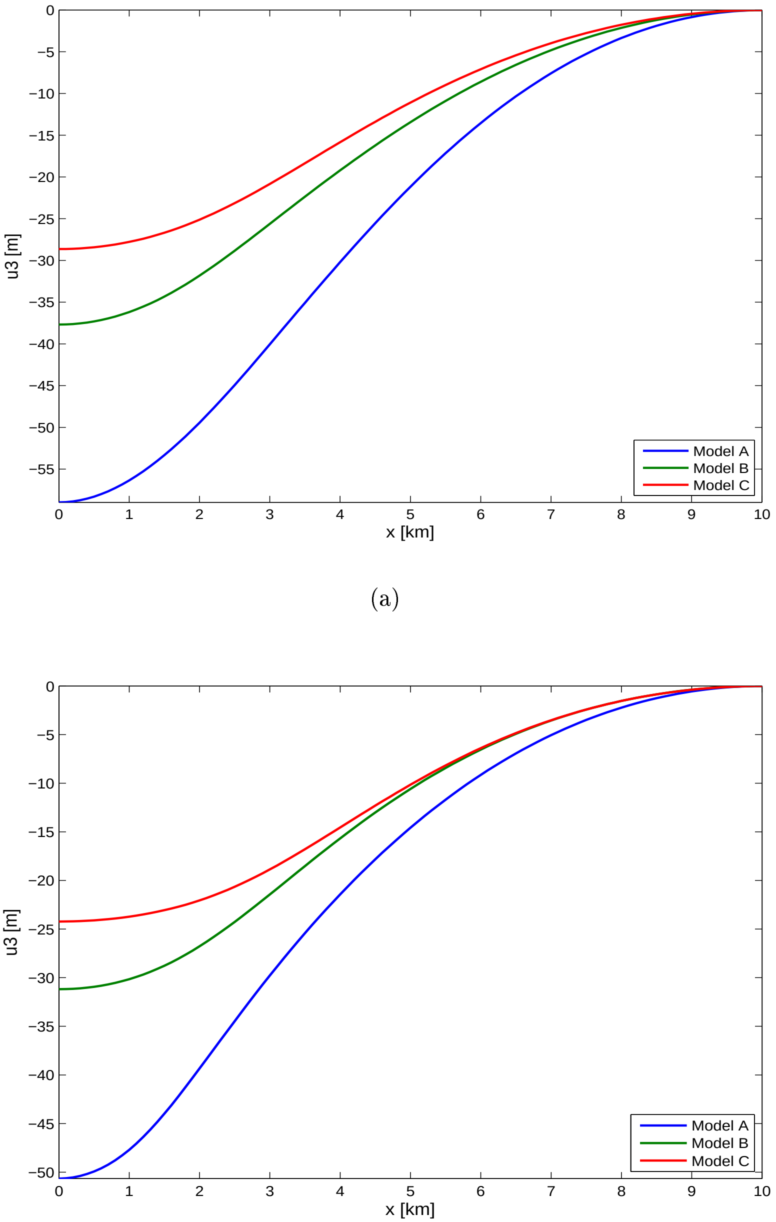

(a)

(b)

Figure 5.14: (a) Vertical displacement results from the temperature dependent models A, B and C. Temperature distribution I in Figure 5.11 was used as initial condition. (b) Vertical displacement results from the temperature dependent models A, B and C. Temperature distribution II in Figure 5.12 was used as initial condition.

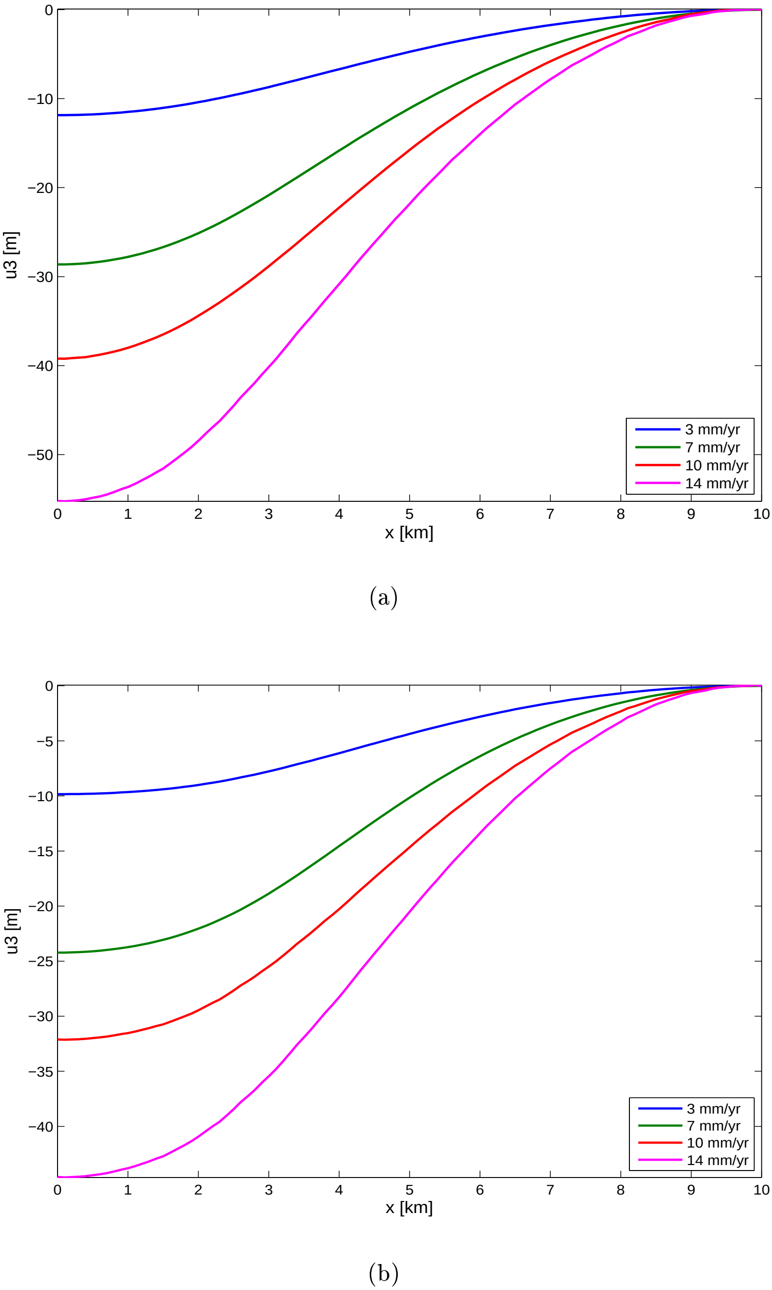

Figure 5.15: Vertical displacement results for model C with spreading rate varied from 3 to 14 mm/yr. In (a) is temperature distribution I (Figure 5.11) used as initial condition and in (b) temperature distribution II (Figure 5.12).

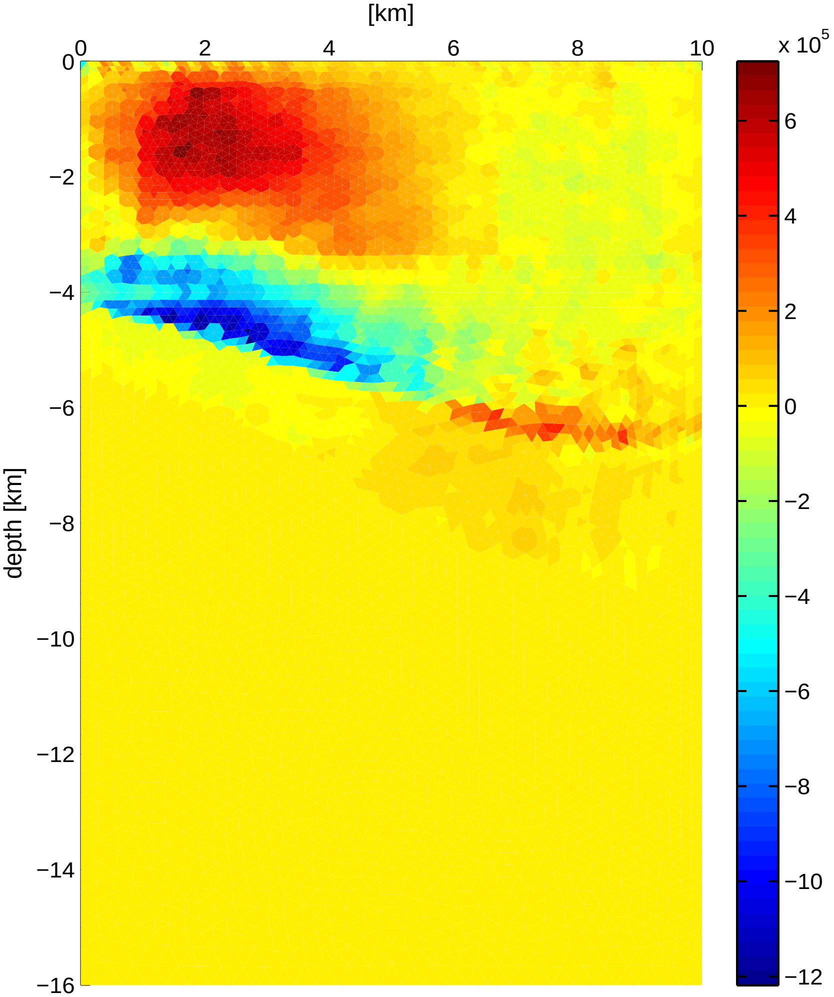

Figure 5.16: Shear stress σ_{13} distribution from model C with temperature distribution according to Figure 5.11 with a maximum ridge temperature of 850°C. The stress values are given in Pa.

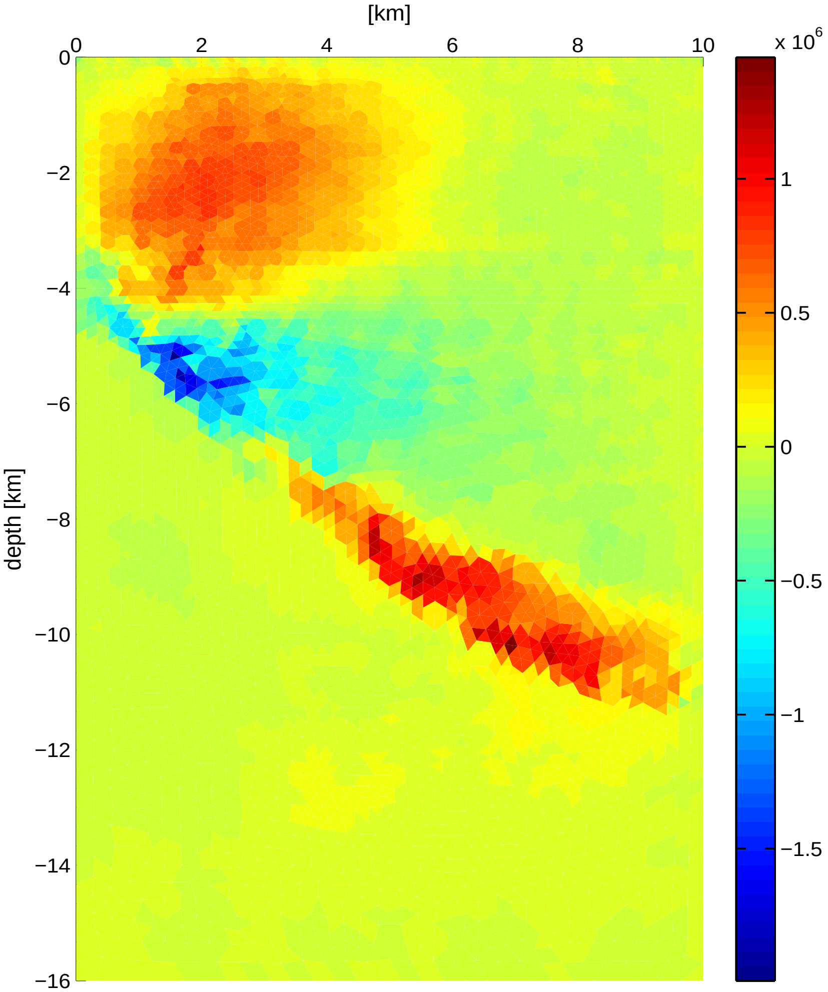

Figure 5.17: Shear stress σ_{13} distribution from model C with temperature distribution according to Figure 5.12 with a maximum ridge temperature of 600°C. The stress values are given in Pa.

6 Evaluation of the models

The aim of the study was to investigate if the amount of subsidence during postglacial time in the Thingvellir graben could to a large degree be the consequence of stretching of plates. The results from this end-member model study, where faulting and dikes were not included, show that about 25–30 m of subsidence can be explained by stretching of the plates. The minimum vertical displacement in Thingvellir during postglacial time is estimated to be about 30 m, measured from fault throws in postglacial lavas (*Sæmundsson*, 1992; *Guðmundsson*, 1987).

The modeling results can also be compared to the rate of vertical displacement from the leveling line measured by *Tryggvason* (1974). Figure 3.3 shows the measured rate of subsidence from 1966 to 1971. In the central part of the graben the subsidence is about 1 mm/yr. However, this value is relative to a reference point about 3–3.5 km away from the central axis of the graben. Thus, the subsidence rate of the central graben relative to a point further away, outside the deformation zone, may be considerably larger. The vertical displacement achieved in the modeling is about 25–30 m (model C) from 10 000 yrs of horizontal stretching, which is equivalent to a subsidence rate of 2.5–3 mm/yr. This value of subsidence of the central graben is relative to a point 10 km away; the width of the model. If instead the subsidence rate of the central part of the model is compared to a point 3–3.5 km away from the central axis, the vertical displacement rate is approximately 1 mm/yr, similar as inferred from the leveling line. The modeling results of subsidence used in the discussion above applies to model C with a temperature dependent rheology.

Plate stretching, considering realistic rheology, may thus have large influence on graben formation at magma-starved rifts. In the following subchapters, the results for each set of models are discussed in detail and thereafter are issues concerning all models discussed.

6.1 Model with an elastic and viscoelastic layer

A comparison of subsidence results from the three rheological models sketched in Figure 4.1, shows that the rheological properties in the model are likely to change non-uniformly with depth, otherwise only a uniform subsidence is achieved over the entire model surface. The model with a uniformly thick elastic layer on top of a viscoelastic layer, is thus oversimplified for a more detailed study of subsidence at a divergent plate boundaries.

The vertical displacement resulting from the variation of model parameters for the models with an elastic and a viscoelastic layer separated by a curved boundary, are shown in Figures 5.4, 5.5 and 5.6. The parameter that has the largest influence on subsidence result is the elastic thickness at the ridge axis. As the elastic thickness h_{axis} is changed one order of magnitude from 500 m to 5000 m, the subsidence decreases by about 20 m. The parameter that has the least influence on subsidence is the viscosity of the viscoelastic layer. As the viscosity is changed by two orders of magnitude from $1{\cdot}10^{18}$ Pa s to $1{\cdot}10^{20}$ Pa s, the resulting model subsidence changes by only $\sim$3 m. Variation of the isotherm temperature, that defines the layer boundary, from 400 to 700°C, gives a decrease in subsidence of about 7 m.

The results show clearly that the amount of vertical subsidence is very sensitive to the depth to a viscous material at the ridge axis. The largest vertical subsidence is achieved with a viscous material at shallow level at the ridge.

Stress analysis

The shear stress focusing, shown in Figures 5.7, 5.8 and 5.9, indicate that an elastic thickness of about 3 km at the ridge axis produces a focusing of shear stress at the surface with its center about 2 km away from the ridge axis. This distance corresponds to the distance from ridge axis to the two marginal faults Almannagjá and Hrafnagjá, respectively. It is reasonable to believe that the large marginal faults are located where the stresses are largest. The stress distribution in the model could hence be used to estimate the thickness of the elastic layer at the ridge axis, and it would be about 3 km according to the result from this study.

The magnitude of the shear stress at the location of focusing is in the range of 50–100 MPa, which is enough to cause faulting according to Amonton's law and Anderson theory of faulting (*Turcotte and Schubert*, 2002).

The appearance of the Thingvellir graben is described by *Sæmundsson* (1992). In the southwest around Lake Thingvallavatn it is narrower, but widens towards northeast. The modeled shear stress distribution, shown in Figures 5.7, 5.8 and 5.9, shows that by increasing the elastic thickness at the ridge, the shear stress focusing at the surface appears further away from the ridge axis. If these results are combined with the observations of widening of the Thingvellir graben, it suggests that the elastic thickness at the ridge axis gets thicker towards northeast. This is equivalent to stating that the crust gets colder towards northeast since the elastic thickness depends on temperature.

6.2 Model with temperature dependent rheology

The modeling of subsidence results in the temperature dependent rheologies, Figure 5.14, shows that the change of temperature distribution affects the subsidence by about 5–10 m. Temperature distribution I (Figure 5.11) with a higher temperature gradient at the ridge axis results in larger vertical displacements.

The uppermost five kilometers in the two temperature distributions have similar thermal structure. Down to 5 km depth, temperature distribution I was defined with a thermal gradient at the ridge axis of 100°C/km resulting in a temperature of 500°C at 5 km depth. Temperature distribution II was defined with a thermal gradient of 100°C/km during the first 2 km and thereafter 70°C/km resulting in a temperature of about 400°C at 5 km depth. This small difference of thermal structure at shallow level results in a small difference of depth to a material with lower viscosity. This may be an explanation why the difference in subsidence is not as large as for the variation of elastic thickness at the ridge axis in the elastic-viscoelastic models. There, the depth to a viscous material was changed from 500 m to 5000 m.

The large difference in temperature between the two temperature distributions occurs first below 5 km and results in the 5–10 m difference in subsidence. The layer of relatively rigid behavior in the first 5 km seems to decrease the effect of the large difference in viscosity at deeper level. The same conclusion as for the elastic-viscoelastic modeling holds also for these models; a viscous material at shallow level affects the subsidence significantly.

Calculation of the effective viscosity for the temperature dependent models A, B and C, as described in Table 5.2, are shown in Table 5.3. The effective viscosity is strongly dependent on temperature, as it changes exponentially with temperature as seen in Equation 5.3. The effective viscosity is also dependent on the differential stress; inversely to the second power. To calculate the effective viscosities for model A, B and C, the differential stress in different temperature intervals was extracted from the model results and put into the effective viscosity equation (Equation 5.3).

Studies of viscosity under Iceland done by *Pagli et al.* (2007) and *LaFemina et al.* (2005) suggest viscosity values of $4\text{–}10{\cdot}10^{18}$ Pa s and $\sim 10^{19}\text{–}10^{20}$ Pa s, respectively. Model A with empirical creep-law values for wet olivine from *Turcotte and Schubert* (2002), gives a calculated maximum effective viscosity of approximately 10^{22} Pa s, for temperature below 250°C. Wet olivine corresponds to a water content of about 0.03 wt % (*Karato and Wu*, 1993). For higher temperatures the effective viscosity decreases even more, as expected. Effective viscosity values for model A appear too low in relation to what could be expected and model A cannot be considered a realistic model. The low values of viscosity is also reflected in the resulting subsidence. Model A predicts 50–60 m of subsidence, depending on temperature distribution, which is about twice as much as all other model results.

Model B and C have empirical creep-law parameters according to dry olivine from *Turcotte and Schubert* (2002) and *Kirby* (1983), respectively. Dry olivine corresponds to water free olivine (*Karato and Wu*, 1993). Both models give large values of the effective viscosity, $>10^{21}$ Pa s, at low temperatures, which is expected. At low temperatures, the crust is rigid and the high viscosity reflects the resistance of the material to deform. The upper, cold parts of the crust are usually assumed to behave purely elastic. The temperature dependent models in this study do not have a purely elastic layer. However, the result for model B and C show that the colder regions in these models deform more or less elastically anyway because of the very high viscosity values.

The effective viscosity values corresponding to higher temperatures for model B and C are lower than estimated in earlier studies of viscosity under Iceland. However, the high temperatures are only located at a small area close to the ridge. Most of the model is defined at temperatures below about 650–700°C and 450–500°C for the two temperature distributions showed in Figures 5.11 and 5.12, respectively. Still, model B gives low values of viscosity. Model C gives values of the viscosity in similar range as *Pagli et al.* (2007) and *LaFemina et al.* (2005) for temperatures between about 450 and 650°C. The transition of effective viscosity values exceeding 10^{21} Pa s occurs at about 450°C for model C. This can be assumed to reflect the change of mechanical properties in the crust, from viscous to elastic.

Hence, rheological model C is the preferable model with high values of the effective viscosity at temperatures below 450°C, reflecting the elastic properties of the crust. It gives viscosity values in accordance with earlier studies for both temperature distributions with the exception of the area close to the ridge for the temperature distribution reaching down to 850°C.

The subsidence result for the favored model C, constructed from a realistic temperature distribution at a divergent plate boundary together with a rheological creep-law behavior according to dry olivine, can be used to give an indication of the subsidence related to stretching of the plates in the WVZ. Figure 5.14 shows the resulting vertical displacement for the two temperature distributions. As discussed in the beginning of this chapter, the subsidence of 25–30 m could describe the measured subsidence in the Thingvellir graben. Both with respect to fault throws within postglacial lavas and subsidence rates from the measured leveling line.

Vertical displacement results for model C with varying spreading rates are shown in Figure 5.15. The results show an approximately linear relationship between spreading rate and subsidence. For temperature distribution I with 850°C as maximum ridge axis temperature, an increase of the spreading rate of 1 mm/yr results in an increase of about

4 m of subsidence. For the colder temperature distribution an increase of the spreading rate of 1 mm/yr results in about 3 m increase of subsidence. These results agree with what is found in the WVZ, where the spreading rates are dependent on latitude. The highest rate is found around Lake Thingvallavatn (*LaFemina et al.*, 2005), as is the largest topographic relief (*Sæmundsson*, 1992). Towards northeast, the spreading rate decreases and the topographic relief is also less pronounced.

Stress analysis

Figures 5.16 and 5.17 show the magnitude of the shear stress in model C for the high and low temperature distribution, respectively. The pattern resembles the result from the elastic-viscoelastic model with a 3 km thick elastic layer at the ridge axis (Figure 5.8). Focusing of the shear stress at the surface is smoothed out between about 1–4 km, but maximum focusing appears at about 2–2.5 km away from the ridge axis. The magnitude of the shear stress is much lower for model C than for the models with an elastic and a viscoelastic layer. Model C only has viscoelastic properties, and even though the effective viscosities in the colder parts of the plate are very high (10^{23} to more than 10^{40} Pa s), the stresses get relaxed. This may explain the discrepancy between the magnitudes of stress. The simplification, made in Chapter 5.1.3, of setting the values of the creep-law parameter A equal to $5{\cdot}10^{-27}$ $\mathrm{Pa}^{-3}\mathrm{yr}^{-1}$ instead of the predicted smaller values, seems to effect the stress levels in the model. If the suggested values of A for low temperatures shown in Figure 5.13, would have been inserted instead, it may have given more realistic values of the shear stress. The best might be to infer purely elastic properties of the colder parts of the model. However, this gives a sharp boundary between an elastic upper layer and a lower viscoelastic layer that probably is not present in the real case.

6.3 General discussion about the model results

All models in this study were of the end-member type where faulting and diking were not taken into account. In reality, there have been rifting events in the Thingvellir area with the most recent one in 1789, when faults north of Lake Thingvallavatn were offset about 1–2 m (*Sæmundsson*, 1992). There was also a smaller slip on Almannagjá of about 9 cm in the 1970ies (*Tryggvason*, 1990). These events with large amounts of instantaneous displacement cannot be explained directly with the end-member models in this study. Nevertheless, a major part of subsidence observed in the Thingvellir graben originates from continuous subsidence resulting from plate spreading, that can be explained by the models in this study. If faulting was included into the models, the effects of the rifting events could be taken into account. The result might be a more stepwise appearance of the subsidence. The faults would probably accommodate most of the subsidence and focus it at their location, instead of the smooth curves of increasing subsidence towards the ridge axis that the end-member models in this study show.

The depth of all models was set to 16 km. This value was chosen from the depth of the isotherms in the models with an elastic-viscoelastic layer. The depth was chosen to be large enough to encompass a viscoelastic layer at the bottom of all models, also for the model with a boundary defined by a higher temperature isotherm. The deepest isotherm from the elastic-viscoelastic models reached down to about 15 km depth, calculated from Equation 5.1 with an isotherm temperature of 700°C and $h_{axis} = 3$ km. For consistency, the calculated depth of 16 km was kept for all models. However, the influence of the depth is only reflected in the total amount of subsidence. A deeper model gives the same subsidence of the ridge axis relative to the intraplate boundary as a shallower.

The modeled vertical displacements were all corrected to have zero subsidence at the intraplate boundary, meaning that the amount of subsidence at this boundary was subtracted from the other result. This can alternatively be viewed as the whole model would have been uplifted the equal amount as the intraplate boundary has subsided during the time of stretching. Buoyancy acting on the plate could explain this uplift. Buoyancy is the upward force on the lighter crust that "floats" on top of the denser mantle (*Turcotte and Schubert*, 2002; *Fowler*, 2005). If the thickness of the crust would change, so would also the vertical location of the crustal layer in accordance with Archimedes' principle. A thinning of the crust in response to stretching would therefore be compensated by uplift due to buoyancy (*Turcotte and Schubert*, 2002). However, the amount of uplift that buoyancy would result in, is difficult to predict since the detailed density profile of the crust is not very well known. For this study it is assumed that buoyancy forces can compensate the subsidence that is seen at the intraplate boundary. Development of the models could be to include gravity and isostatic compensation.

In addition to the results already showed and discussed, model C was also run with a lower value of the elastic parameter Young's modulus to test the influence on subsidence. Results from *Grapenthin et al.* (2006) suggest a value of Young's modulus of 40 ± 15 GPa from modeling of snow load in Iceland and seasonal changes in GPS data. However, the vertical subsidence in model C was not effected by the lowering of Young's modulus from 90 GPa to 40 GPa. It seems like the parameter that has the least influence on subsidence is the elastic and viscous properties, such as Young's modulus and viscosity, that is tested in this study.

7 Conclusions

The main conclusion from this study is that plate stretching, without diking, can to a large degree explain the formation of graben structures at magma-starved rifts. The rheological model that is needed to fit with the geological constraints, should have rheological properties that change non-uniformly with depth. Otherwise, the modeling results only in a uniform subsidence and uniformly distributed stress levels. This is observed in the results from the initial model tested in this study with a horizontal elastic layer on top of a viscoelastic layer.

The largest vertical displacements for the models with a curved boundary between an elastic upper layer and a viscoelastic lower layer, are achieved when a viscoelastic material is found close to the surface at the ridge axis. The thickness of the elastic layer is not known, but the results from shear stress focusing give an indication of an elastic ridge axis thickness of 3 km. This thickness results in about 23 m of subsidence from the combined elastic and viscoelastic model. The viscosity of the viscoelastic layer is of little importance for the subsidence result.

A combination of the resulting shear stress distribution and observations of widening of the Thingvellir graben suggests that the elastic layer at the ridge axis gets thicker towards northeast. Modeling results show that a thicker elastic layer at the ridge axis produces less subsidence, which is also in accordance with geological observations of less topographic relief toward northeast in the Thingvellir graben. These results suggest a colder crust towards northeast, since elastic thickness depends on temperature.

Among the temperature dependent models, model C is the preferable one, with calculated effective viscosity values in the range that is expected in relation to earlier studies. The subsidence for this model is 25–30 m depending on which temperature distribution that is used as initial condition. The result is equivalent to the measured minimum throws of faults within postglacial lavas in the Thingvellir graben (*Sæmundsson*, 1992; *Guðmundsson*, 1987). The result is also in accordance with vertical displacement rates measured on the leveling line north of Lake Thingvallavatn (*Tryggvason*, 1974).

The variation of spreading rate effects the subsidence approximately linearly. For the temperature distribution with a higher temperature gradient at the ridge axis, an increase of spreading rate of 1 mm/yr results in an increase of about 4 m in subsidence. For the temperature distribution with a lower temperature gradient at the ridge axis, an increase of spreading rate of 1 mm/yr results in an increase of about 3 m in subsidence. Thus, the effect of spreading rate on topography is large and can explain much of the difference of topographic relief found in Thingvellir graben.

Results for shear stress focusing from model C, show the same pattern as for the elastic-viscoelastic models. However, the values are unrealistically low. This is a consequence of the lack of purely elastic properties in the upper part of the model.

A development of this study could be to combine temperature dependent rheologies for both elastic and viscoelastic properties, giving a model that shows purely elastic properties in the colder parts and viscoelastic properties for higher temperatures. The assumption of buoyancy that was used to justify the correction of subsidence at the intraplate boundary, also need to be further investigated in a future study.

Finally, this study shows that to a large degree stretching of the plates at a divergent plate margin can explain the formation of graben structures at magma-starved rifts. Moreover, it shows how the combination of an inferred colder crust and the decay of subsidence with decreasing spreading rate, can explain the decreasing topographic relief and widening of the Thingvellir graben towards northeast.

Finally, this study shows that to a large degree stretching of the plates at a divergent plate margin can explain the formation of graben structures at magma-starved rifts. It also gives an explanation of the decreasing topographic relief, and widening of the Thingvellir graben towards northeast by combining the results from the shear stress distribution and the dependency of subsidence on spreading rate.

References

Abaqus (2007), Abaqus documentation, version 6.7.

Batchelor, G. (1980), *An Introduction to Fluid Dynamics*, Cambridge Univ. Press, Cambridge.

Bernauer, F. (1943), *Junge Tektonik auf Island und ihre Ursachen, in Spalten auf Island*, 14-64 pp., Wittwer, K., Stuttgart, Germany.

Bjarnason, I. Th. and Menke, W. and Flóvenz, Ó. and Caress, D. (1993), Tomographic image of the Mid-Atlantic Plate Boundary in southwestern Iceland, *J. Geophys. Res.*, *98*, 6607–6622.

Björnsson, A. (2007), Temperature of the Icelandic crust: Inferred from electrical conductivity, temperature surface gradient, and maximum depth of earthquakes, *Tectonophysics*, doi:10.1016/j.tecto.2006.02.027.

Bull, J., T. Minshull, N. Mitchell, K. Thors, J. Dix, and A. Best (2003), Fault and magmatic interaction within Iceland's western rift over the last 9 kyr, *Geophys. J. Int.*, *154*, F1–F8.

DeMets, C., R. Gordon, D. Argus, and S. Stein (1990), Current plate motions., *Geophys. J. Int.*, *101*, 425–478.

DeMets, C., R. Gordon, D. Argus, and S. Stein (1994), Effect of recent revisions to the geomagnetic reversal time scale on estimates of current plate motions, *Geophys. Res. Lett.*, *21*, 2191–2194.

Desai, C., and T. Kundu (2001), *Introductory Finite Element Method*, CRC Press LLC, Florida.

Einarsson, P., and K. Sæmundsson (1987), Earthquake epicenters 1982-1985 and volcanic systems in Iceland, in: Th. Sigfusson (ed.), *I hlutarins edli: Festschrift for Thorbjorn Sigurgeirsson*, Menningarsjodur, Reykjavik [map].

Flóvenz, O., and K. Sæmundsson (1993), Heat flow and geothermal processes in iceland, *Tectonophysics*, *225*, 123–138.

Flügge, W. (1975), *Viscoelasticity*, 2nd ed., Springer-Verlag, Berlin.

Foulger, G. (1995), The Hengill geothermal area, Iceland: Variation of temperature gradients deduced from the maximum depth of seismogenesis, *J. Volcanol. Geotherm. Res.*, *155*, 567–590.

Fowler, C. (2005), *The Solid Earth*, 2nd ed., Cambridge Univ. Press, Cambridge.

Fung, Y. (1965), *Foundations of Solid Mechanics*, Prentice-Hall, Inc., New Jersey.

Goetze, C. (1978), The mechanisms of creep in olivine, *Phil. Trans. R. Soc. Lond.*, *288*, 99–119.

Grapenthin, R., F. Sigmundsson, H. Geirsson, T. Árnadóttir, and V. Pinel (2006), Icelandic rhytmics: Annual modulation of land elevation and plate spreading by snow load, *Geophys. Res. Lett.*, *33*, L24305, doi:10.1029/2006GL028081.

Guðmundsson, A. (1987), Tectonics of the Thingvellir fissure swarm, SW Iceland, *Journ. Structural Geology*, *9*(1), 61–69.

Haflidason, H., G. Larsen, and G. Ólafsson (1992), The recent sedimentation history of Thingvallavatn, Iceland, *Oikos*, *64*, 80–95.

Jakobsson, S. (1979), Petrology of recent basalts of the Eastern Volcanic Zone, Iceland, *Acta Nat. Island.*, *26*, 1–103.

Kaban, M., O. Flóvenz, and G. Pálmason (2002), Nature of the crust-mantle transition zone and the thermal state of the upper mantle beneath Icleand from gravity modelling, *Geophys. J. Int.*, *149*, 281–299.

Karato, S., and P. Wu (1993), Rheology of the upper mantle: A synthesis, *Science*, *260*(5109), 771–778, doi:10.1126/science.260.5109.771.

Karato, S., M. Paterson, and J. Fitzgerald (1986), Rheology of synthetic olivine aggregates - influence of grain size and water, *J. Geophys. Res.*, *91*, 8151–8176.

Kirby, S. (1983), Rheology of the lithosphere, *Rev. Geophys.*, *21*, 1458–1487.

Kirby, S., and A. Kronenberg (1987), Rheology of the lithosphere: selected topics, *Rev. Geophys.*, *25*, 1219–1244.

Kjartansson, G. (1964), Geological map of Iceland, sheet 5, central Iceland, Mus. of Nat. Hist., Dep. of Geol. and Geogr., Reykjavík.

LaFemina, P., T. Dixon, R. Malservisi, T. Árnadóttir, E. Sturkell, F. Sigmundsson, and P. Einarsson (2005), Geodetic GPS measurements in south Iceland: Strain accumulation and partioning in a propagating ridge system, *J. Geophys. Res.*, *110*, B11405, doi: 10.1029/2005JB003675.

Menke, W., and D. Sparks (1995), Crustal accretion model for Iceland predicts 'cold' crust, *Geophys. Res. Lett.*, *22*(13), 1673–1676.

Menke, W., V. Levin, and R. Sethi (1995), Seismic attenuation in the crust at the mid-Atlantic plate boundary in south-west Iceland, *Geophys. J. Int.*, *122*(1), 175–182, doi:10.1111/j.1365-246X.1995.tb03545.x.

Ólafsdóttir, R. (2007), Institue of Earth Sciences, University of Iceland, personal communication.

Pagli, C., F. Sigmundsson, B. Lund, E. Sturkell, H. Geirsson, P. Einarsson, T. Árnadóttir, and S. Hreinsdóttir (2007), Glacio-isostatic deformation around the Vatnajökull ice cap, Iceland, induced by recent climate warming: GPS observations and finite element modeling, *J. Geophys. Res.*, *112*, B08405, doi:10.1029/2006JB004421.

Pálmason, G., and K. Sæmundsson (1979), Summary of heat flow in Iceland. In: Cermak, Rybach (Eds.), Terrestrial heat flow in Europe. Springer, Berlin, Heidelberg.

Ranalli, G. (1995), *Rheology of the Earth*, 2nd ed., Chapman & Hall, London.

Sæmundsson, K. (1978), Fissure swarms and central volcanoes of the neovolcanic zones of Iceland, in: D.R Bowes and B.E. Leake (eds), Crustal evolution in NW-Britain and adjacent regions, *Geol. J.*, *10*, 415–432.

Sæmundsson, K. (1979), Outline of the geology of Iceland, *Jökull*, *29*, 7–28.

Sæmundsson, K. (1992), Geology of the Thingvallavatn area, *Oikos*, *64*, 40–68.

Sigmundsson, F. (2006), *Iceland Geodynamics: Crustal Deformation and Divergent Plate Tectonics*, Springer-Verlag, London.

Sigmundsson, F., P. Einarsson, R. Bilham, and E. Sturkell (1995), Rift-transform kinematics in south Iceland: Deformation from Global Positioning System measurements, 1986 to 1992, *J. geophys. Res.*, *100*(B4), 6235–6248.

Sinton, J., K. Grönvold, and K. Sæmundsson (2005), Postglacial eruptive history of the Western Volcanic Zone, Iceland, G^3, *6*, Q12009, doi: 10.1029/2005GC001021.

Stefánsson, R., et al. (1993), Earthquake prediction research in the south Iceland seismic zone and the SIL project, *Bull. Seismol. Soc. Am.*, *83*(3), 696–716.

Thors, K. (1992), Bedrock, sediments, and faults in Thingvallavatn, *Oikos*, *64*, 69–79.

Tryggvason, E. (1974), Vertical crustal movements in iceland, in *Geodynamics of Iceland and the North Atlantic Area*, edited by Kristjansson, pp. 241–262, Reidel, Dordrecht.

Tryggvason, E. (1990), Höggun Almannagjár. Mælingar á Thingvöllum 1990, Nordic Volcanological Institute, Report 9001.

Tsenn, M., and N. Carter (1987), Upper limit of power law creep of rocks, *Tectonophysics*, *136*, 1–26.

Turcotte, D., and G. Schubert (2002), *Geodynamics*, 2nd ed., Cambridge Univ. Press.

Watts, A. (2001), *Isostasy and Flexure of the Lithosphere*, Cambridge Univ. Press.

Wu, P. (2004), Using commercial finite element packages for the study of earth deformations, sea levels and the state of stress, *Geophys. J. Int.*, *158*, 401–408, doi:10.11 11/j.1365-246X.2004.02338.x.

Appendix A Physical background

Continuum mechanics and rheology provide the tools to investigate the physical mechanisms behind the geological formations caused by spreading at divergent plate boundaries.

In continuum mechanics a body is divided into elemental volumes that act in a continuous way. This means that the body does not break and that neighboring elemental volumes remain as neighbors also when exposed to external forces (*Fung*, 1965; *Ranalli*, 1995). Differences at atomic level are generalized to have no influence on the properties of each elemental volume.

Rheology describes how materials are deformed due to an applied stress. Both intrinsic parameters such as viscosity or bulk modulus, specific for a certain material, and external parameters such as temperature, pressure or duration of the applied stress, affects the rheology of a material (*Ranalli*, 1995). The duration of the applied stress is especially essential and materials that act elastically in short time scales may start to flow when exposed to stresses for longer time. There are many different types of relations between applied stress and material response. The end members of these rheologies are elastic and viscous behavior, respectively. In an elastic media, an applied stress causes an instantaneous deformation that is fully recovered as the stress is relieved. In a fluid, the flow caused by an applied stress is not reversible and in the simplest form of a fluid, a Newtonian fluid, the applied stress is proportional to the rate of deformation.

A material that flows when subjected to a constant stress is defined in rheology as a fluid irrespective of the internal structure of the atoms (*Ranalli*, 1995). For one and the same material this may vary with e.g. temperature, pressure or time of applied stress.

The dynamic and the kinematic states of a continuous body are in rheology expressed in stress and strain, respectively. They can be related to each other through constitutive equations. These equations differ depending on the rheology of the material. The general form of a constitutive equation can be written as (*Ranalli*, 1995)

$$R(\varepsilon, \dot{\varepsilon}, \sigma, \dot{\sigma}, \ldots, \{M\}) = 0 \tag{A.1}$$

where ε is the strain, σ is the stress, a dot defines time derivative, $\{M\}$ represents the material parameters and R is called the rheological function.

A.1 Stress

Two types of forces act in a continuous body; body forces, force per unit volume or mass, and surface forces, force per unit area bounding the body (*Turcotte and Schubert*, 2002). The traction, also called the stress vector, on a surface is defined as the limiting case of the force acting on the surface divided by the surface as it goes to zero (*Ranalli*, 1995)

$$T_{(n)i} = \lim_{\delta S \to 0} \frac{\delta F_i}{\delta S} \tag{A.2}$$

where $T_{(n)i}$ is the traction on the surface δS with outer normal vector $n = 1,\ 2,\ 3$ pointing in the direction $x_1,\ x_2,\ x_3$ respectively. δF is the force that acts upon δS. The traction $T_{(n)i}$ depends both on the forces acting upon the surface and the direction of the surface. The traction $T_{(n)i}$ can be divided into one normal and two tangential components to the surface. When the traction for each surface is divided into its components, these can be put together to form the stress tensor. The stress tensor can be written as (*Ranalli*, 1995)

$$\sigma_{ij} = \begin{pmatrix} T_{(1)j} \\ T_{(2)j} \\ T_{(3)j} \end{pmatrix} = \begin{pmatrix} \sigma_{11} & \sigma_{12} & \sigma_{13} \\ \sigma_{21} & \sigma_{22} & \sigma_{23} \\ \sigma_{31} & \sigma_{32} & \sigma_{33} \end{pmatrix} \tag{A.3}$$

where the first subscript of the stress tensor σ_{ij} refers to the direction of the outer surface normal. The second subscript refers to the direction in which the stress component acts. The on-diagonal components of the stress tensor are called normal stresses and the off-diagonal are called shear stresses. If a coordinate system is oriented in such a way so that all shear stresses that act on a body are zero, the body is said to be in a principal stress state (*Turcotte and Schubert*, 2002). In that case the stress tensor only has non-zero on-diagonal components which are called principal stresses.

In many cases, only the stresses that differ from the hydrostatic case are of interested. Then it is an advantage to separate the stress tensor into two parts, the isotropic part and the deviatoric part (Equation A.4). The isotropic part is the mean normal stress and the deviatoric part represents the stresses that differ from the pure hydrostatic state of stress (*Fung*, 1965)

$$\sigma_{ij} = \sigma_0 \delta_{ij} + \sigma^{'}_{ij} \tag{A.4}$$

where $\sigma_0 = \frac{1}{3}\sigma_{kk} = -p$ which is the average of the normal stresses and also the lithostatic pressure p, $\sigma^{'}_{ij}$ denotes the deviatoric stress and δ_{ij} is the Kronecker delta.

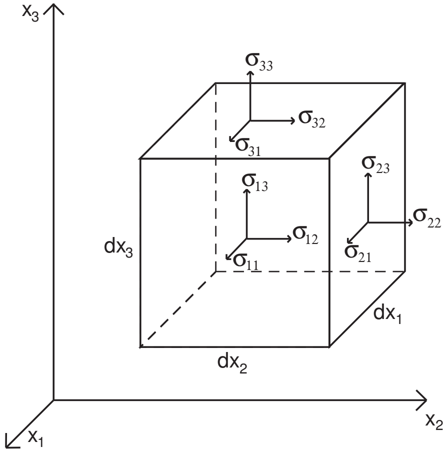

Figure A.1: All stress components that act on an infinitesimal cube.

The positive direction of stress is defined (in continuum mechanics) to be the same as the direction of the outer surface normal (*Fung*, 1965; *Ranalli*, 1995). Therefore, tensional stresses are positive whereas compressional stresses are negative. The SI unit for stress is *pascal* [Pa].

The state of stress in a continuous body can be examined through a force balance on an infinitesimal parallelepiped inside the media. If the body is in equilibrium, the resultant from the force balance in each coordinate direction will be zero. The governing equations, called the equilibrium equations (Equation A.5), are valid for all types of rheology.

$$\frac{\partial \sigma_{ji}}{\partial x_j} + \rho X_i = 0 \tag{A.5}$$

where ρ is the density of the material and X_i is the body force acting along coordinate axis i. However, since there are more unknowns than equations they need to be put together with a proper constitutive equation in the form of Equation A.1 (*Ranalli*, 1995).

If the body is in equilibrium, moments also have to add up to zero otherwise there is a non-zero net moment causing the body to rotate, and the body would not be in equilibrium. When the moments about an axis parallel to each of the axis x_1, x_2 and x_3 of the infinitesimal cube showed in Figure A.1 are set to zero, the results prescribes symmetry of the stress tensor i.e. $\sigma_{ij} = \sigma_{ji}$ (*Ranalli*, 1995; *Fung*, 1965).

A.2 Strain

Strain is related to deformation of a body. When a force acts on a continuous body the particles inside it will be displaced. They can be displaced both with respect to each other (deformed) and to an outer reference point i.e., they can be deformed, translated and/or rotated (*Ranalli*, 1995). Two neighboring particles inside the body will be dis-

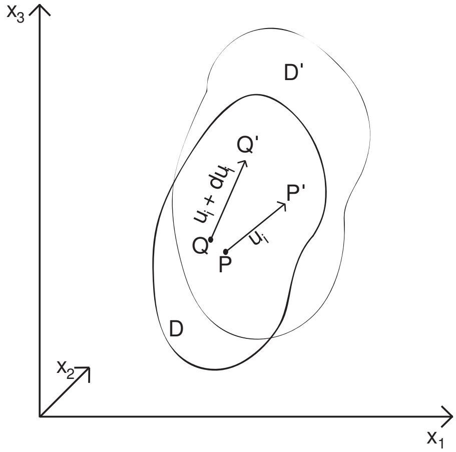

Figure A.2: Displacement of the two particles P and Q to P' and Q'.

placed differently if not only rigid body translation and rotation occurs. The difference in displacement of the two particles P and Q in Figure A.2 can be written as

$$\mathrm{d}u_i = \frac{\partial u_i}{\partial x_j}\mathrm{d}x_j \tag{A.6}$$

where $\mathrm{d}u_i$ is the difference in displacement of the two particles, $\mathrm{d}x_j$ is the initial distance between the particles and $\frac{\partial u_i}{\partial x_j}$ are the displacement gradients. With the assumption that the first derivatives of the displacements are very small, the difference between Lagrangian (material) and Eulerian (spatial) derivatives can be neglected (*Ranalli*, 1995; *Fung*, 1965). The displacement gradient in Equation A.6 can then be expanded into Equation A.7. From this equation is the infinitesimal strain tensor defined (Equation A.8) (*Ranalli*, 1995).

$$\frac{\partial u_i}{\partial x_j} = \frac{1}{2}\left(\frac{\partial u_i}{\partial x_j} + \frac{\partial u_j}{\partial x_i}\right) + \frac{1}{2}\left(\frac{\partial u_i}{\partial x_j} - \frac{\partial u_j}{\partial x_i}\right) \tag{A.7}$$

$$\varepsilon_{ij} \equiv \frac{1}{2}\left(\frac{\partial u_i}{\partial x_j} + \frac{\partial u_j}{\partial x_i}\right) \tag{A.8}$$

From Equation A.8 it can be seen that the strain tensor is symmetric, $\varepsilon_{ij} = \varepsilon_{ji}$ (*Ranalli*, 1995). The second term in Equation A.8 is called the rigid-body rotation and is antisymmetric.

In the same way as with the stress tensor are the on-diagonal components of the strain tensor called normal strains and the off-diagonal components called shear strains. When the coordinates system is oriented in such a way so that only the normal strains are non-zero, the strain elements are called principal strains. The strain tensor can also be divided into an isotropic and a deviatoric part as the with the stress tensor (*Ranalli*, 1995):

$$\varepsilon_{ij} = \frac{1}{3}\theta\delta_{ij} + \varepsilon_{ij}^{'} \tag{A.9}$$

where $\theta = \varepsilon_{kk}$ is called the cubical dilatation and $\varepsilon_{ij}^{'}$ is the deviatoric strain.

The strain tensor gives six equations for only three unknowns, u_1, u_2 and u_3. This means that it is an overdetermined system and for the solution to be single-valued the strain components ε_{ij} need to fulfill the compatibility equations (*Fung*, 1965). In 3D there are six additional compatibility equations, but for a simplified case with plane strain only one equation of compatibility remains that can be written as

$$\frac{\partial^2 \varepsilon_{11}}{\partial x_2^2} + \frac{\partial^2 \varepsilon_{22}}{\partial x_1^2} = 2\frac{\partial^2 \varepsilon_{12}}{\partial x_1 \partial x_2} \tag{A.10}$$

Plane strain

In some situations one or two of the principal stress or strain components can be assumed to be zero (*Turcotte and Schubert*, 2002). In plane strain one of the principal strain components is zero. In the modeling of the Thingvellir graben, plane strain conditions are assumed to be valid. Most of the deformation occurs along the direction of spreading and in the vertical direction and the deformation along the rift axis is assumed to be negligible.

A.3 Elasticity

Many materials behave elastically at low temperatures and pressures. They deform instantaneously as a stress is applied, as the load is removed, the body recovers completely to its initial shape. The relation between applied stress and strain in a continuous elastic media has been observed to be linear and is described by Hooke's law (Equation A.11), where C_{ijkl} is the 4^{th} order tensor of elastic parameters (*Fung*, 1965). Hooke's law is the constitutive equation for an elastic medium and is written as

$$\sigma_{ij} = C_{ijkl}\varepsilon_{kl} \tag{A.11}$$

In this, the most general form of Hooke's law, C_{ijkl} has 21 independent elastic parameters. It is reduced from 81 parameters because of i.a. symmetry of the stress and strain tensors (*Fung*, 1965). In an isotropic media, Hooke's law is simplified and only two elastic constants remain as see in in Equation A.12.

$$\sigma_{ij} = \lambda\varepsilon_{kk}\delta_{ij} + 2\mu\varepsilon_{ij} \tag{A.12}$$

where λ and μ are the two remaining elastic parameters from the 4^{th} order tensor C_{ijkl}, called the Lamé's constants (*Ranalli*, 1995).

Lamé's constants are two of five elastic parameters commonly used to describe the properties of an elastic material. The five parameters are (*Turcotte and Schubert*, 2002; *Fung*, 1965)

λ – the *Lamé parameter*. No physical meaning, but can be used for writing equations in a concise way.

μ – the *modulus of rigidity* or the *shear modulus*. The ratio of shear stress to shear strain, hence describing how the material reacts to shearing stresses.

E – *Young's modulus* or the *modulus of elasticity*. A measure of the stiffness of a material.

υ – *Poisson's ratio*. Describes the material response when stretched or compressed in one direction and consequently decreases or increases in the other two directions.

K – the *bulk modulus*. A measure of how a material's volume changes with pressure.

However, only two of the five parameters are independent.

To be able to solve for the displacements u_i that occur in a continuous elastic media under loading, the equations of equilibrium need to be extended to the equations of motion and combined with Hooke's law. The resulting equations are called the *Cauchy-Navier equations* and is a set of partial differential equations in terms of the displacements u_i.

So the first step to get to the Cauchy-Navier equations is to rewrite the equations of equilibrium A.5 as the equations of motion where the net forces in the system do not necessary need to sum up to zero. D'Alembert's principle which is the equivalent to Newton's second law in continuum mechanics, states that the resultant of forces in a system are equal to the time derivative of the linear momentum. If the displacements and velocities are small, the difference in the Lagrangian and Eulerian derivatives can be ignored and the equations of motion ca be written as

$$\frac{\partial \sigma_{ij}}{\partial x_j} + \rho X_i = \rho a_i = \rho \ddot{u}_i \tag{A.13}$$

where a_i is the acceleration. Double dots denote second time derivative. The second step is to insert the relation of stress and strain from Hooke's law into the equations of motion. This gives the Cauchy-Navier equations and with a change of order how derivatives are taken, they can be written as (*Ranalli*, 1995)

$$(\lambda + \mu)\frac{\partial \theta}{\partial x_i} + \mu \nabla^2 u_i + \rho X_i = \rho \frac{\partial^2 u_i}{\partial t^2} \tag{A.14}$$

where $\theta = \varepsilon_{kk}$ is the cubical dilatation and $\nabla^2 = \frac{\partial^2}{\partial {x_i}^2}$ is the Laplacian operator.

An example – stretching of plate

The horizontal extension accommodated by the 20 km wide deformation zone at Thingvellir is approximately 70 m during Postglacial time (see chapter 3). If symmetry of the graben is assumed, two 10 km wide zones with 35 m of horizontal deformation at each side of the ridge axis can model the plate boundary. The thickness of the elastic layer can be estimated from earthquake hypocenter data, since most earthquakes occur only in elastic media. This suggests a seismogenic layer of about 7 km thickness (*Stefánsson et al.*, 1993; *Foulger*, 1995). If the plate is assumed to behave elastically the resulting vertical displacement from 35 m of pulling can be calculated from the relation of stress and strain components in an elastic medium, which can be written as (*Ranalli*, 1995)

$$\begin{aligned} \varepsilon_{ij} &= \frac{1}{E}((1+\nu)\sigma_{ij} - \nu \sigma_{kk}\delta_{ij}) \\ \sigma_{ij} &= \lambda \varepsilon_{kk}\delta_{ij} + 2\mu\varepsilon_{ij} \end{aligned} \tag{A.15}$$

With the assumption of plane strain ε_{22} is equal to zero which gives $\sigma_{22} = \nu(\sigma_{11} + \sigma_{33})$. For Poisson's ratio $\nu = 0.5$ it can be shown from Equation A.15 that the horizontal and vertical strains are equal in size but with opposite signs, $\varepsilon_{11} = -\varepsilon_{33}$. The vertical displacement for the elastic plate after 35 m horizontal extension with Poisson's ratio equal to 0.5 is

$$u_{33} = \varepsilon_{33}h = -\varepsilon_{11}h = \frac{u_{11}}{L}h = -24.5 \text{ m} \tag{A.16}$$

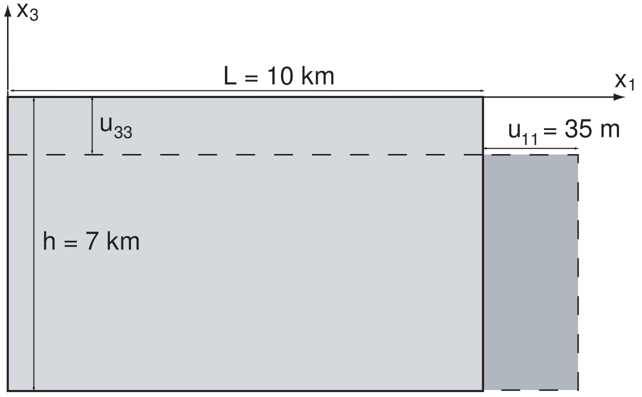

Figure A.3: Sketch of the elastic plate with length $L = 10$ km and depth $h = 7$ km which is stretched 35 m horizontally.

A more realistic value of Poisson's ratio for the lithosphere is 0.25 (*Watts*, 2001; *Turcotte and Schubert*, 2002) and for this case the vertical displacement in the plate from a 35 m horizontal pull is

$$\begin{aligned} \varepsilon_{33} &= -\frac{\varepsilon_{11}}{2.9924} = -1.17 \cdot 10^{-3} \\ u_{33} &= \varepsilon_{33} h = -8.19 \text{ m} \end{aligned}$$

where ε_{33} is found from multiplying ε_{11} with the ratio of the strain components related to Poisson's ratio $\nu = 0.25$. The ratio of ε_{11} and ε_{33} for an arbitrary stress state and Poisson's ratio varying from 0 to 0.5 is shown in Figure A.4.

This analytical result can be compared to the resulting value from a numerical computation in Abaqus. As seen in Figure A.5, the analytical and numerical result of the vertical subsidence from 35 m of horizontal stretching and Poisson's ratio $\nu = 0.25$, is in accordance.

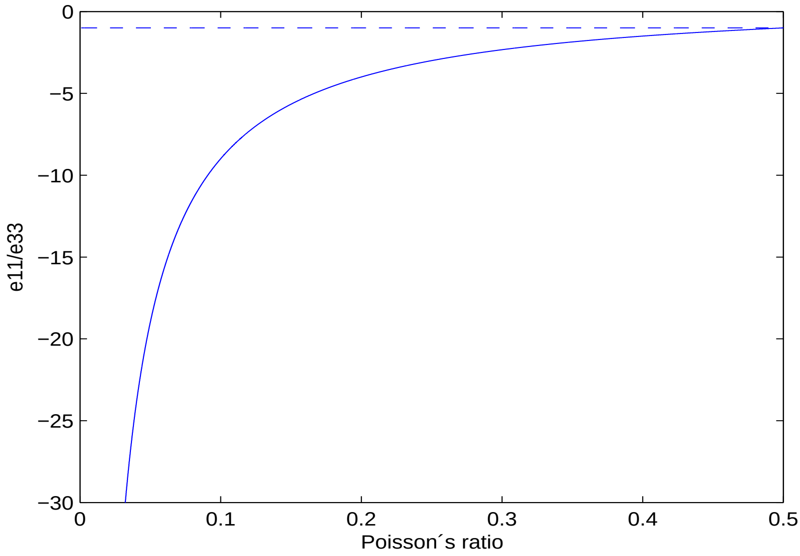

Figure A.4: The ratio of horizontal strain ε_{11} and vertical strain ε_{33} plotted for Poisson's ratio varying between 0 and 0.5.

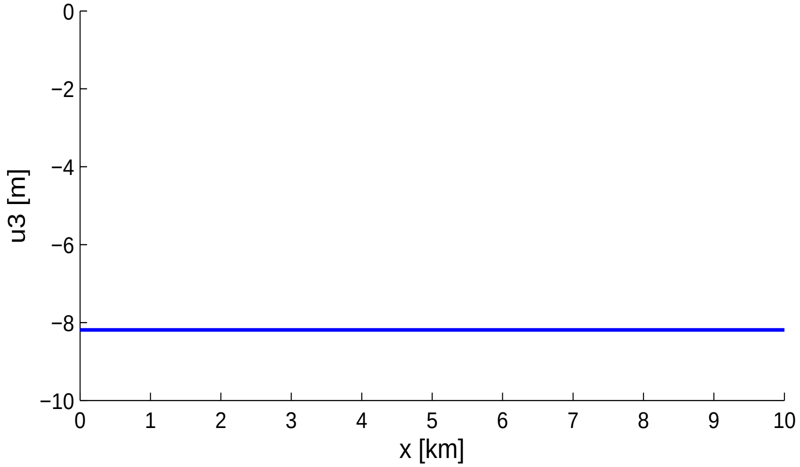

Figure A.5: Subsidence of an elastic plate as calculated in Abaqus. The resulting subsidence is 8.19 m from 35 m horizontal stretching. Thus, the same as derived from the analytical calculation. The width of the plate was 10 km and the depth was 7 km. Poisson's ratio was 0.25.

A.4 Fluids

There are two classes of fluids; Newtonian and non-Newtonian. The simplest case is materials with a Newtonian rheology where the stress is linearly proportional to the strain rate (*Ranalli*, 1995). But experimental results suggest that many Earth materials have a non-linear relationship between stress and strain rate.

For materials with elastic behavior the kinematic state was described by strains, displacements and the displacement gradient; for fluids it is described by strain rate, velocities and velocity gradients. Similar to the elastic case where the strain tensor was defined, a strain rate tensor $\dot{\varepsilon}_{ij}$ can be defined from velocities and their gradients as (*Ranalli*, 1995)

$$\dot{\varepsilon}_{ij} = \frac{\mathrm{D}\varepsilon_{ij}}{\mathrm{D}t} = \frac{1}{2}\left[\frac{\mathrm{D}}{\mathrm{D}t}\left(\frac{\partial u_i}{\partial x_j}\right) + \frac{\mathrm{D}}{\mathrm{D}t}\left(\frac{\partial u_j}{\partial x_i}\right)\right] = \frac{1}{2}\left(\frac{\partial v_i}{\partial x_j} + \frac{\partial v_j}{\partial x_i}\right) \tag{A.17}$$

where second order terms of the velocity gradient $\frac{\partial v_i}{\partial x_j}$ are ignored and $\frac{\mathrm{D}}{\mathrm{D}t}$ denotes the Lagrangian (material) derivative.

To obtain the equations of motion for a Newtonian fluid, the procedure resembles the steps done for an elastic rheology. One major difference is that fluid pressure enters the equations. As stated above for a Newtonian fluid, the stress is linearly related to the strain rate and from symmetry of the stress and strain rate tensors and for an isotropic media, the relation can be written as (*Ranalli*, 1995; *Fung*, 1965)

$$\sigma_{ij} = -p\delta_{ij} - \frac{2}{3}\eta\dot{\theta}\delta_{ij} + 2\eta\dot{\varepsilon}_{ij} \tag{A.18}$$

where p is the fluid pressure, $\dot{\theta} = \dot{\varepsilon}_{kk}$ and η is the material parameter called the *viscosity*. In a state of stress where the normal stresses are all compressive or tensional and equal in magnitude, the constitutive equation for a Newtonian fluid can be rewritten in terms of only deviatoric stress related to deviatoric strain rate. This is done by substituting Equation A.4 and the equivalence to Equation A.9 but for strain rate into Equation A.18 which gives

$$\sigma'_{ij} = 2\eta\dot{\varepsilon}'_{ij} \tag{A.19}$$

The viscosity η, which relates the deviatoric shear stress linearly to the deviatoric shear strain rate, describes the material's ability to flow. This relation applies for shear stress only; the relation of normal stress to strain rate for a Newtonian fluid is $\sigma_{ij} = 3\eta\dot{\varepsilon}_{ij}$ $(i = j)$ (*Ranalli*, 1995). Thus the definition of viscosity for a state of normal stress and strain in a Newtonian fluid is (*Ranalli*, 1995)

$$\eta = \frac{\sigma_{ij}}{3\dot{\varepsilon}_{ij}}, \; (i = j) \tag{A.20}$$

Typical values of viscosity under Iceland are estimated from glacio-isostatic deformation to be $4\!-\!10 \cdot 10^{18}$ Pa s (*Pagli et al.*, 2007). Modeling done by *LaFemina et al.* (2005) of deformation from GPS measurements in the EVZ and WVZ give higher viscosities, $10^{19} - 10^{20}$ Pa s.

As in the elastic case, the equations of motion are set up by balancing forces to the rate of change of the linear momentum. If the stress in the force balance is substituted by the relation from Equation A.18 and a change of order of derivation is made, the equations of motion for a Newtonian fluid can be written as (*Ranalli*, 1995)

$$-\frac{\partial p}{\partial x_i} + \frac{1}{3}\eta\frac{\partial}{\partial x_i}\left(\frac{\partial v_j}{\partial x_j}\right) + \eta\nabla^2 v_i + \rho X_i = \rho\frac{\mathrm{D}v_i}{\mathrm{D}t} \tag{A.21}$$

The equations of motion for a Newtonian rheology are called the *Navier-Stokes equations.* In some situations, these equations can be simplified. E.g., if the fluid is incompressible, it can be shown from conservation of mass that $\frac{\partial v_i}{\partial x_i} = 0$, and this term disappears in the Navier-Stokes equations (*Fung*, 1965). The assumption of incompressibility also suggests that the fluid pressure p can be written as $p = p_0 + \rho X_i + P$ where $p_0 + \rho X_i$ refers to the fluid pressure at rest and P is the pressure from fluid motion (*Batchelor*, 1980). This rewriting removes the gravity from the Navier-Stokes equations. Furthermore, the material acceleration $\frac{\mathrm{D}v_i}{\mathrm{D}t}$ of particles can be neglected for highly viscous material as e.g. mantle material (*Turcotte and Schubert*, 2002). These simplifications modify the Navier-Stokes equations into the shorter form written as

$$-\frac{\partial P}{\partial x_i} + \eta\nabla^2 v_i = 0 \tag{A.22}$$

Non-Newtonian fluids

One form of non-Newtonian material behavior is the power-law dependency between strain rate and stress that is described by (*Ranalli*, 1995; *Turcotte and Schubert*, 2002)

$$\dot{\varepsilon} = A\sigma^n \tag{A.23}$$

where A is a parameter that depends on both intrinsic and extrinsic properties and n defines the power-law relation between strain rate $\dot{\varepsilon}$ and stress σ.

The viscosity of non-Newtonian fluids can be defined in the same way as for Newtonian fluids for normal stress and strain rate as

$$\eta = \frac{\sigma}{3\dot{\varepsilon}} \tag{A.24}$$

but if the power-law relation between strain rate and stress from Equation A.23 is inserted into Equation A.24, this gives that the viscosity for non-Newtonian fluids is dependent on stress. The non-Newtonian viscosity is called the effective viscosity and can be written as (*Turcotte and Schubert*, 2002; *Ranalli*, 1995)

$$\eta_{eff} = \frac{1}{3A}\sigma^{1-n} \tag{A.25}$$

A.5 Viscoelasticity

The upper part of the crust acts in most cases as an elastic material (*Turcotte and Schubert*, 2002), but for lower parts of the crust and the mantle the behavior of the Earth must be explained with another rheology. In short time-scales ($< 10^4\ s$), seen from seismic wave studies, the effect is still elastic but for longer time-scales ($\sim 10^4\ yrs$), seen from e.g. postglacial rebound, the lower crust-upper mantle flows (*Ranalli*, 1995; *Turcotte and Schubert*, 2002). This type of rheology is described by viscoelasticity which is the sum of an elastic and a viscous rheology. A linear viscoelastic body can be described in a mechanical way to consist of a spring and a dash-pot. The spring represents the instantaneous deformation due to elastic properties of the body and the dash-pot represents the long-term deformation from the fluid flow (*Flügge*, 1975; *Fung*, 1965).

When the spring and the dash-pot is placed in series as shown in Figure A.6(a) they represent the behavior of a viscoelastic material called a Maxwell body (*Flügge*, 1975). The elastic strain and the viscous strain is then added together to get the total deformation of the body, see Figure A.6(b). The relation between applied stress and strain for a Maxwell body is linear, but the cumulative deformation for a viscoelastic material also depends on the time history of the applied stress (*Fung*, 1965; *Flügge*, 1975). Viscoelastic materials can also be non-linear if a non-Newtonian stress-strain rate relationship is used as the viscous contribution.

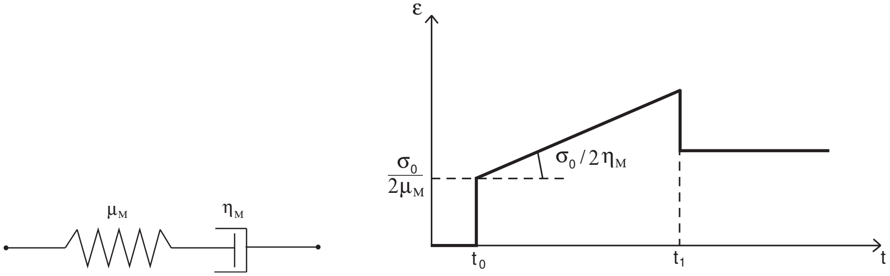

(a) (b)

Figure A.6: (a) The mechanical analogue of a viscoelastic material with a spring and a dash-pot. (b) Graph of the strain versus time in a Maxwell viscoelastic body with the instantaneous elastic strain and the linear viscous strain rate.

The relationship between uniaxial stress and strain for an elastic and a Newtonian material can be written as

$$\sigma = E\varepsilon_E \tag{A.26}$$

$$\sigma = 2\eta\dot{\varepsilon}_V \tag{A.27}$$

To get the total deformation for a Maxwell body the elastic and the viscous contribution are added together. Since the stress is related to strain rate in a Newtonian fluid, Equation A.26 is differentiated with respect to time so that the total strain rate can be written as the sum of the elastic $\dot{\varepsilon}_E$ and the viscous strain rate $\dot{\varepsilon}_V$ (*Ranalli*, 1995; *Flügge*, 1975).

$$\dot{\varepsilon} = \dot{\varepsilon}_E + \dot{\varepsilon}_V = \frac{\dot{\sigma}}{E} + \frac{\sigma}{2\eta} \tag{A.28}$$

where E is Young's modulus and η is the viscosity. If the strain is kept constant so that $\dot{\varepsilon} = 0$, Equation A.28 can be solved for the stress σ. This can be written as (*Turcotte and Schubert*, 2002; *Flügge*, 1975)

$$\sigma = \sigma_0 e^{-\frac{E}{2\eta}t} \tag{A.29}$$

where σ_0 is the initial stress and t is time. $\frac{3\eta}{E}$ is called the Maxwell relaxation time τ_M and refers to the time it takes for the stress σ in the viscoelastic material to decrease to 1/e of the initial stress σ_0, under the condition of constant strain.

Appendix B Finite element modeling

In finite element modeling (FEM) the continuous world that surrounds us is discretized to simplify calculations. The results from all discretized parts are added together to get the result for the whole continuous body. The parts obtained after discretization of a continuous body, are called finite elements. For two dimensional problems there are two kinds of element types; quadrilateral or triangular elements (*Desai and Kundu*, 2001). The size and shape of the elements are defined with a mesh. At the nodal points, that are placed at the corners but if necessary from accuracy requirements also along the sides of an element, the values of the unknown variables are calculated. Two neighboring elements must have the same value of the unknowns in a shared nodal point. Otherwise, the continuity of the body collapses (*Desai and Kundu*, 2001). Since unknowns only are calculated at the nodal points and then interpolated to get values between points, the result for the whole body is only an approximation to the continuous case. Depending on the geometry of the body and the required accuracy of the solution the mesh size can be adjusted to fit the demands of the problem.

According to *Desai and Kundu* (2001) the method of solving problems with finite elements can be divided into a series of steps. First the continuous body needs to be discretized as discussed above and then constitutive equations must be specified e.g. Hooke's law to relate stress and strain for an elastic material. These constitutive equations which applies to the continuous case are then transformed to element equations. The element equations give the constitutive relationships for each nodal point. To get the total result for the whole body the element equations are calculated and added together for all elements of the body and assembled into the global equations. Boundary conditions are set to constrain the problem. Finally the unknowns can be found from the global equations by use of Gaussian elimination. Gaussian elimination is an algorithm used to find the solutions of a system of linear equations.

B.1 Abaqus

Abaqus is a commercial software for finite element calculations. Models can be created either completely in the Abaqus viewer or scripts can be used to read in models into Abaqus. Abaqus can also receive and directly run input files written in the object oriented programming language python. The output is written to an output database which, in the same way as the input, can either be visualized in Abaqus viewer or the data can be read into e.g. Matlab for plotting.

To create a model in Abaqus the following things needs to be defined

1. Geometry of the part/parts in the model
2. Material properties
3. Sections if the part consists of different materials
4. Part instances and an assembly
5. Time steps
6. Boundary conditions and loads
7. Mesh and element types
8. Output variables
9. Job to run the input file

The models in this study were made by two-dimensional planar shells of unit thickness. The different types of elements that exist in Abaqus are showed in Figure B.1.

A viscoelastic material in Abaqus is created by defining a material with both elastic and viscous properties. Young's modulus and Poisson's ratio specify the elastic properties and a strain-hardening creep law relates to the viscous behavior. The creep law for a Maxwell body is given as (*Abaqus*, 2007)

$$\dot{\varepsilon} = \Big(A\sigma^n[(m+1)\varepsilon]^m\Big)^{\frac{1}{m+1}} \tag{B.1}$$

where A is a material parameter, n defines the power law relation between strain rate and stress for the material and m defines the power of strain hardening. With $m = 0$ it follows that Equation B.1 is equivalent to the power law relation for non-Newtonian materials (Equation A.23).

For a Maxwell viscoelastic material, stress is linearly related to strain

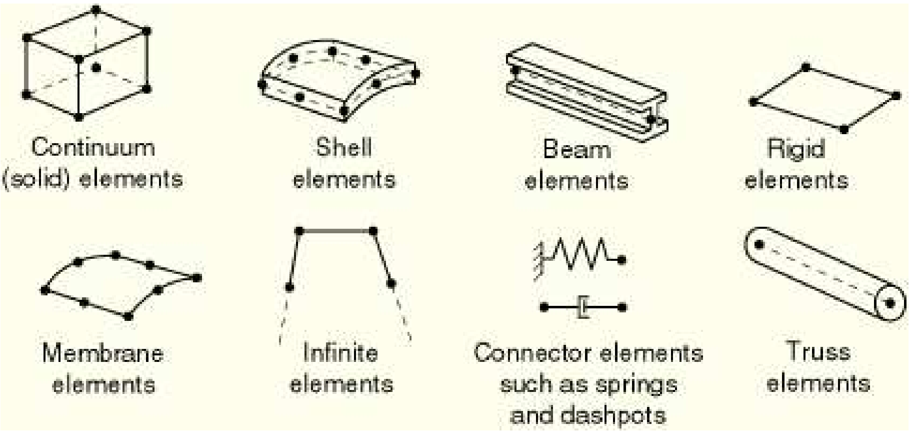

Figure B.1: Overview of the different element types that are available in Abaqus (*Abaqus*, 2007). The shell element is used for the models in this study

rate and hence n equals one in the above equation. By substituting the Abaqus creep law, with no strain-hardening, into the definition of viscosity for uniaxial conditions (Equation A.24), the parameter A is determined as

$$A = \frac{1}{3\eta} \tag{B.2}$$

In cases with non-Newtonian materials can the parameter A in Equation B.1 be determined from experimental data. If the creep law given in Abaqus is compared with the empirical power-law relation given in Equation 4.2 it follows that A is given as

$$A = A_p e^{-H/RT} \tag{B.3}$$

where A_p is a material-specific parameter, H is the activation energy, R is the universal gas constant, and T is the temperature in Kelvin.

Appendix C Values of parameter A

A [$\mathrm{Pa}^{-3}\mathrm{yr}^{-1}$]	T [°C]
$5 \cdot 10^{-27}$	<200
$8.68 \cdot 10^{-19}$	300
$2.15 \cdot 10^{-13}$	400
$2.14 \cdot 10^{-9}$	500
$2.59 \cdot 10^{-6}$	600
$7.28 \cdot 10^{-4}$	700
$7.15 \cdot 10^{-2}$	800

Table C.1: Specification of the values given in Abaqus for the creep parameter A with varying temperature according to empirical values of A_p, $H = 398$ kJ mol^{-1} and $n = 3$ corresponding to wet Olivine (*Turcotte and Schubert*, 2002)

A [$\mathrm{Pa}^{-3}\mathrm{yr}^{-1}$]	T [°C]
$5 \cdot 10^{-27}$	<300
$5.52 \cdot 10^{-22}$	400
$9.23 \cdot 10^{-17}$	500
$9.83 \cdot 10^{-13}$	600
$1.56 \cdot 10^{-9}$	700
$6.24 \cdot 10^{-7}$	800

Table C.2: Specification of the values given in Abaqus for model B for the creep parameter A with varying temperature according to empirical values from *Turcotte and Schubert* (2002) for dry Olivine. $H = 520$ kJ mol^{-1} and $n = 3$

A [$\mathrm{Pa}^{-3}\mathrm{yr}^{-1}$]	T [°C]
$5 \cdot 10^{-27}$	<400
$1.50 \cdot 10^{-22}$	500
$1.59 \cdot 10^{-18}$	600
$2.52 \cdot 10^{-15}$	700
$1.01 \cdot 10^{-12}$	800

Table C.3: Specification of the values given in Abaqus for model C for the creep parameter A with varying temperature according to empirical values from *Kirby* (1983). $H = 520$ kJ mol^{-1} and $n = 3$